J. Fluid Mech. (1991), *vol.* 223, *pp.* 209–240
Printed in Great Britain

Responses to topographical forcing

By WOLFGANG FENNEL AND MARTIN SCHMIDT
Academy of Sciences of GDR, Institute of Marine Research, Rostock-Warnemünde, DDR-2530

(Received 3 August 1989 and in revised form 2 July 1990)

The influence of small topographic features on the dynamic responses of an inviscid, stratified, f-plane ocean to a time-dependent upstream flow is studied. Based on the quasi-geostrophic vorticity equation we analyse a quasi-nonlinear approach, in which the horizontal currents in the advection terms are replaced by the upstream flow. It appears that the quasi-nonlinear theory is susceptible to analytical treatment and contains the essential dynamics to give a sufficient description of the response scenario. As examples, infinitely long ridges and a right-circular cylinder are considered. In the case of an infinitely long top-hat ridge closed-form expressions can be derived. In the case of a cylindrical obstable the theory gives explicit indications of which term corresponds to which of the processes involved, such as topographic waves, which are generated in the starting phase and move clockwise round the obstacle, vortex shedding, and formation of a vortex over the cylinder in the final steady state.

1. Introduction

This paper re-examines the effects of small topographic features on the dynamics of a stratified, rotating fluid on an f-plane. In particular, the oceanic response to a current U_0 flowing over a topographic obstable is analysed in the framework of the quasi-geostrophic theory, i.e. high-frequency processes such as inertial waves are filtered out.

There are various studies of this type of problem, with and without stratification, assuming f-plane or β-plane dynamics, e.g. Hogg (1973), Huppert (1975), McCartney (1975), Huppert & Bryan (1976), Johnson (1984), Willmott (1984), Verron (1986), Gill *et al.* (1986), Verron, Provost & Holland (1987), Killworth (1989), and references therein.

Most of those papers are based on numerical experiments whereas analytical solutions are known only for some special cases, such as the linear approximation (Johnson 1984) and the nonlinear steady state (Hogg 1973; Huppert 1975). Moreover, Huppert & Bryan (1976), H & B hereafter, used a very simplified analytical model to discuss qualitatively some aspects of the results of their numerical simulations. To our knowledge analytical approximations covering the whole response scenario, i.e. the generation of topographic waves, vortex shedding and, finally, the formation of Taylor columns have not been reported in the literature.

It is the aim of the present paper to attack this problem. Our analytical investigations are focused on a quasi-nonlinear approach, where a Green's-function technique can be used to study the response scenarios at topographic features. As examples we consider infinitely long ridges and a cylindrical obstable.

The case where the upstream current flows over an infinitely long ridge,

perpendicular to its axis is relatively simple but has the virtue that in the case of a flat-topped ridge closed-form expressions of the topographically induced response can be obtained. Such solutions may serve as a kind of reference case in the analysis of more complex situations.

If a current, suddenly switched on and being constant thereafter, flows over a cylindrical obstacle two processes, topographic waves and vortex shedding, determine the response scenario. Initially a topographic wave is excited, moving clockwise round the obstacle. Later, owing to advective processes, a cyclonic vortex is shed, while an anticyclonic vortex remains over the obstacle. The advection time emerges as an important timescale which is defined by $T_a = L/U_0$, where U_0 is the upstream velocity and L is the lateral scale of the obstacle. For small times, $t \ll T_a$, topographic waves dominate the response, while for $t \approx T_a$ the vortex shedding becomes important. For times much larger than the advection time, $t \gg T_a$, a steady state is established where the streamlines of the topographically induced currents are parallel to f/H contours. An excellent description of this scenario was provided by the numerical simulations in H & B.

The paper is organized as follows; in §2 we briefly summarize the basic equations, and in §3 a source representation for the topographically induced pressure is derived for the linear, the quasi-nonlinear and the nonlinear stationary approximation. Section 4 describes the dynamic effects of an infinite ridge and §§5 and 6 are devoted to the response produced by a right-circular topographic feature.

2. Basic equations

Ignoring high-frequency processes, such as inertial waves, we can describe the response of currents to small topographic features in terms of the quasi-geostrophic vorticity equation

$$\mathrm{D}_t \zeta = 0. \tag{2.1}$$

The potential vorticity ζ is related to the pressure p by the potential equation

$$\zeta = (\mathscr{L} + \nabla^2) p, \tag{2.2}$$

where

$$\mathscr{L} = \frac{\partial}{\partial z}\frac{f^2}{N^2}\frac{\partial}{\partial z}, \quad \nabla^2 = \frac{\partial^2}{\partial x^2} + \frac{\partial^2}{\partial y^2}.$$

f is the inertial frequency and N the Brunt–Väisälä frequency. The symbol D_t stands for

$$\mathrm{D}_t = \frac{\partial}{\partial t} + \boldsymbol{u}\cdot\boldsymbol{\nabla}. \tag{2.3}$$

Using the geostrophic equations

$$u = -\frac{1}{f} p_y, \quad v = \frac{1}{f} p_x \tag{2.4}$$

(2.3) can be rewritten as

$$\mathrm{D}_t = \frac{\partial}{\partial t} + \frac{1}{f} J(p, \ldots) \tag{2.5}$$

where $J(a, b) = a_x b_y - a_y b_x$ is the Jacobian.

At the surface we use the boundary condition

$$\mathrm{D}_t\left(p_z + \frac{N^2}{g} p\right) = 0 \quad \text{for} \quad z = 0. \tag{2.6a}$$

The bottom boundary condition is that there is no flow normal to the bottom boundary, $z = -H(\boldsymbol{r})$, i.e.

$$\mathrm{D}_t p_z = \frac{N^2}{f} J(p, H) \quad \text{for} \quad z = -H(\boldsymbol{r}). \tag{2.6b}$$

The bold $\boldsymbol{r}$ denotes the horizontal radius vector $\boldsymbol{r} = (x, y)$ with

$$r = |\boldsymbol{r}| = (x^2 + y^2)^{\frac{1}{2}}.$$

We consider an ocean of constant depth H_0, which is disturbed by topographic features such as seamounts, valleys or ridges described by a profile function $h(\boldsymbol{r})$. Then, the total depth is given by

$$H(\boldsymbol{r}) = H_0 - h(\boldsymbol{r}). \tag{2.7}$$

If a large-scale upstream current $\boldsymbol{u}_0$ flows over the feature a topographically induced response will be generated. Thus, the pressure p consists of two parts, an upstream contribution p_0 due to the flow $\boldsymbol{u}_0$ and the topographically forced response ψ,

$$p = p_0 + \psi. \tag{2.8}$$

In particular, for a homogeneous upstream flow in the x-direction p_0 is

$$p_0 = -f u_0(t)\, y.$$

Far upstream we require ψ to vanish

$$\psi \to 0 \quad \text{for} \quad x \to -\infty. \tag{2.9}$$

In the following the analysis is confined to small topographic heights, i.e. $h/H \ll 1$. This implies that the solution of the set (2.6) can be obtained by means of a perturbation theory. For a geostrophic upstream pressure our basic equations reduce to

$$\mathrm{D}_t(\mathscr{L} + \nabla^2)\psi = 0, \tag{2.10}$$

$$\mathrm{D}_t(\psi_z + \frac{N^2}{g}\psi) = 0 \quad \text{for} \quad z = 0, \tag{2.11a}$$

$$\mathrm{D}_t \psi_z = -\frac{N^2}{f} J(\psi, h) - N^2 \boldsymbol{u}_0 \cdot \nabla h \quad \text{for} \quad z = -H(\boldsymbol{r}). \tag{2.11b}$$

Since h is independent of time (2.11b) can be rewritten as

$$\mathrm{D}_t(\psi_z + N^2 h) = 0 \quad \text{for} \quad z = -H(\boldsymbol{r}). \tag{2.12}$$

Equation (2.1) states that the vorticity ζ is conserved along streamlines and since it vanishes far upstream, it remains zero everywhere,

$$(\mathscr{L} + \nabla^2)\psi = 0.$$

Thus, the evolution of ψ with time is determined only by the boundary conditions (2.11).

3. Formal solution of the quasi-geostrophic equation

The quasi-geostrophic equation (2.10) together with the boundary conditions (2.11) form a nonlinear set which can only be solved numerically. However, in some cases which correspond to certain stages of the evolution of the response function ψ

an analytical treatment is possible. We use a Green's-function method which is outlined in this section. This method can be considered as a generalization of that used in H & B. In particular we examine the linear, nonlinear stationary and the quasi-nonlinear approximations. The corresponding Green's functions are evaluated explicitly in Appendix A.

3.1. *The linear approximation*

Let the upstream flow be switched on suddenly at $t = 0$. As long as the time t is small compared to the advection time T_a we can expect a linear response, i.e. for $t \ll T_a$ we replace D_t by $\partial/\partial t$ and find from (2.10), (2.11 *a*, *b*)

$$\frac{\partial}{\partial t}(\nabla^2 + \mathscr{L})\,\psi^L(\boldsymbol{r}, z, t) = 0, \tag{3.1}$$

and

$$\frac{\partial}{\partial t}\left(\psi^L_z - \frac{N^2}{g}\psi^L\right) = 0 \quad \text{for} \quad z = 0, \tag{3.2a}$$

$$\frac{\partial}{\partial t}\psi^L_z = -N^2(\boldsymbol{u}\cdot\nabla h) = -N^2(\boldsymbol{u}_0\cdot\nabla h) - \frac{N^2}{f}J(\psi^L, h) \quad \text{for} \quad z = -H. \tag{3.2b}$$

The superscript L indicates the linear approximation of ψ.

We introduce a Green's-function L which corresponds to ψ^L and is defined by

$$-\frac{\partial}{\partial t'}(\mathscr{L}' + \nabla^{2'})\,L(\boldsymbol{r}, z, t, \boldsymbol{r}', z', t') = \delta(\boldsymbol{r}-\boldsymbol{r}')\,\delta(z-z')\,\delta(t-t'). \tag{3.3}$$

The primed operators denote differentiation with respect to the primed variables of L. We require the boundary conditions

$$\frac{\partial}{\partial t'}\left(L_{z'} + \frac{N^2}{g}L\right) = 0 \quad \text{for} \quad z' = 0. \tag{3.4a}$$

$$\frac{\partial}{\partial t'}L_{z'} = 0 \quad \text{for} \quad z' = -H, \tag{3.4b}$$

$$L \to 0 \quad \text{for } r' \to \infty \tag{3.5a}$$

and

$$L = 0 \quad \text{for} \quad t < t'. \tag{3.5b}$$

The calculation of the Green's function is given in Appendix A. Once the Green's function is known a source representation can be derived in the usual manner to obtain

$$\psi^L(\boldsymbol{r}, z, t) = -f^2 \int \mathrm{d}\boldsymbol{r}' \int_0^t \mathrm{d}t' L(\boldsymbol{r}, z, t; \boldsymbol{r}', -H, t')\left(\boldsymbol{u}_0\cdot\nabla' h + \frac{1}{f}J(\psi^L(\boldsymbol{r}', -H, t'), h)\right). \tag{3.6}$$

This linear integro-differential equation reveals that the flow perpendicular to the contour lines of the topographic feature is the source of the induced pressure response ψ^L. Since friction is ignored no stationary state for ψ^L exists and we anticipate that the initial phase of the response to a flow $\boldsymbol{u}_0$ governed by (3.6) is dominated by topographic waves.

In order to investigate qualitatively the effect of dissipation one can formally

include Rayleigh friction and Newton cooling by replacing $\partial/\partial t$ by $\partial/\partial t+\nu$, where for simplicity the same friction constant ν is used for both processes. In this manner the form of (3.6) is retained, but the Green's function L will be multiplied by an additional factor $e^{-\nu(t-t')}$.

3.2. *The nonlinear stationary state*

In the opposite case of large times, i.e. $t \gg T_a$, the response is in a steady state. Replacing D_t in (2.10), (2.11a), and (2.12) by $(1/f)J(p,\ldots)$ we obtain the equation

$$J(p,\zeta)=0 \tag{3.7}$$

and the boundary conditions

$$J\left(p,\frac{N^2}{g}p+p_z\right)=0 \quad \text{for} \quad z=0 \tag{3.8a}$$

and

$$J\left(p,\frac{p_z}{N^2}+h\right)=0 \quad \text{for} \quad z=-H. \tag{3.8b}$$

From general properties of the Jacobian together with the upstream condition (2.9) this set can be integrated along streamlines and reduces to

$$(\mathscr{L}+\nabla^2)\psi^S=0 \tag{3.9}$$

with the boundary conditions

$$\psi^S_z=-\frac{N^2}{g}\psi^S \quad \text{for} \quad z=0, \quad \psi^S_z=-N^2h \quad \text{for} \quad z=-H. \tag{3.10a, b}$$

The solution of the boundary-value problem (3.9) and (3.10a, b) can be expressed also by means of a source representation

$$\psi^S(\boldsymbol{r},z)=-f^2\int \mathrm{d}\boldsymbol{r}'h(\boldsymbol{r}')\,S(\boldsymbol{r},z;\boldsymbol{r}',-H), \tag{3.11}$$

where S is the associated Green's function defined as

$$(\mathscr{L}'+\nabla^{2\prime})\,S(\boldsymbol{r},z,\boldsymbol{r}',z')=\delta(\boldsymbol{r}-\boldsymbol{r}')\,\delta(z-z'), \tag{3.12}$$

with the boundary conditions

$$S_{z'}+\frac{N^2}{g}S=0 \quad \text{for} \quad z'=0, \tag{3.13}$$

$$S_{z'}=0 \quad \text{for} \quad z'=-H. \tag{3.14}$$

This solution expresses the fact that in the stationary case the streamlines of the topographically induced current are parallel to f/H contours. Moreover, ψ^S turns out to be independent of the upstream flow $\boldsymbol{u}_0$. Thus, (3.11) describes the stationary final state of the topographically induced pressure for an arbitrary background flow, seemingly independent of history and spatial structure of $\boldsymbol{u}_0$.

Inserting the examples of $h(\boldsymbol{r})$ used in Hogg (1973) and Huppert (1975) equation (3.11) would give their results.

3.3. *The quasi-nonlinear approximation*

For times of the order of T_a the linear approximation is no longer applicable and the advective terms in (2.10) and (2.11a, b) must be taken into account. This is indicated

by the fact that for large times the linear approximation (3.6) does not converge to the stationary state (3.11). It is one purpose of this paper to show that a quasi-nonlinear approach connects the linear approximation and the nonlinear stationary state, i.e. it contains both of them as limit cases. This implies that a quasi-nonlinear approximation gives a good description of the whole response scenario.

In the quasi-nonlinear approximation the operator D_t has to be replaced by

$$\mathrm{D}_t \approx \mathscr{D}_t = \frac{\partial}{\partial t} + \boldsymbol{u}_0 \cdot \nabla, \tag{3.15}$$

i.e. only the upstream flow is retained in the advective terms. The quasi-nonlinear system has the virtue that, as in the linear case, the solutions can be expressed in terms of a Green's function. With (3.15) we rewrite the quasi-geostrophic equation (2.10) as

$$\mathscr{D}_t(\nabla^2 + \mathscr{F})\,\psi(\boldsymbol{r}, z, t) = 0. \tag{3.16}$$

The associated Green's function is governed by

$$(\nabla^{2\prime} + \mathscr{F}')\,\bar{\mathscr{D}}_{t'} G(\boldsymbol{r}, z, t; \boldsymbol{r}', z', t') = \delta(\boldsymbol{r} - \boldsymbol{r}')\,\delta(z - z')\,\delta(t - t'), \tag{3.17}$$

where $\bar{\mathscr{D}}_t$ is the adjoint operator of $\mathscr{D}_t$

$$\bar{\mathscr{D}}_t = -\frac{\partial}{\partial t} - \nabla \cdot \boldsymbol{u}_0. \tag{3.18}$$

The definition of the Green's function G by means of (3.17) appears to be convenient to derive a source representation for ψ also for the more general case where $\boldsymbol{u}_0$ also depends on $\boldsymbol{r}$ or z.

We multiply (3.16) by G, (3.17) by ψ, add the resulting equations and integrate to obtain

$$\psi(\boldsymbol{r}, z, t) = \int \mathrm{d}\boldsymbol{r}' \int_{-H}^{0} \mathrm{d}z' \int_{-\infty}^{\infty} \mathrm{d}t' [\psi((\nabla^{2\prime} + \mathscr{F}')\,\bar{\mathscr{D}}_{t'} G) - G(\mathscr{D}_{t'}(\nabla^{2\prime} + \mathscr{F}'))\,\psi].$$

The operator $\mathscr{D}_t$ in the second term can be integrated by parts where $\psi = 0$ for $t' \to -\infty$, $G = 0$ for $t' \to \infty$, and $G \to 0$ for $r' \to \infty$ were required. It can easily be seen that the terms with the horizontal Laplacian $\nabla^{2\prime}$ give no contribution, i.e. only the terms associated with $\mathscr{F}'$ remain. After integration by parts with respect to z' these terms can be written as

$$\psi(\boldsymbol{r}, z, t) = \int \mathrm{d}\boldsymbol{r}' \int_{-\infty}^{\infty} \mathrm{d}t' \frac{f^2}{N^2} \left(\psi \frac{\partial}{\partial z'} \bar{\mathscr{D}}_{t'} G - (\bar{\mathscr{D}}_{t'} G) \frac{\partial}{\partial z'} \psi \right) \Bigg|_{-H}^{0}.$$

We choose the boundary conditions for the Green's function G as

$$\left(\frac{\partial}{\partial z'} + \frac{N^2}{g} \right) \bar{\mathscr{D}}_{t'} G = 0 \quad \text{for} \quad z' = 0, \tag{3.19a}$$

$$\frac{\partial}{\partial z'} \bar{\mathscr{D}}_{t'} G = 0 \quad \text{for} \quad z' = -H. \tag{3.19b}$$

Then it appears that only the bottom boundary condition at $z = -H$ yields a non-vanishing contribution and we arrive at the following integro-differential equation for ψ:

$$\psi(\boldsymbol{r}, z, t) = -f^2 \int \mathrm{d}\boldsymbol{r}' \int \mathrm{d}t' G(\boldsymbol{r}, z, t; \boldsymbol{r}', -H, t') \left(\boldsymbol{u}_0 \cdot \nabla' h + \frac{1}{f} J(\psi, h) \right), \tag{3.20}$$

where (2.11 b) with D_t replaced by $\mathscr{D}_t$ has been used.

3.4. *Discussion and implications of the integral equation*

Equation (3.20) together with the definition of the Green's function is a rather general expression for ψ. In particular, it is difficult to evaluate the Green's function G explicitly for an arbitrary background flow $\boldsymbol{u}_0$. Nevertheless (3.20) permits some insight in the evolution of the response pattern.

Formally, (3.20) is equivalent to the linear approximation (3.6); however, it differs in the Green's function. Obviously, (3.20) reduces to the linear integro-differential equation (3.6) if the quasi-nonlinear terms in the Green's functions are dropped, i.e.

$$G(\boldsymbol{r}, z, t, \boldsymbol{r}', z', t') = L(\boldsymbol{r}, z, t, \boldsymbol{r}', z', t') \quad \text{for} \quad \boldsymbol{u}_0 \to 0. \tag{3.21}$$

Moreover the stationary state as given by (3.11) can also be derived from (3.20). In order to show this we have to investigate the properties of the Green's function in more detail. Writing the causality condition explicitly by means of a step function

$$G(t, t') = \theta(t-t')\, K(t, t')$$

it follows that

$$\bar{\mathscr{D}}_{t'} G(t, t') = \delta(t-t')\, K(t, t') - \bar{\theta}(t-t')\, \mathscr{D}_{t'} K(t, t'). \tag{3.22}$$

From (3.22) together with (3.17) we find

$$(\mathscr{L}' + \nabla^{2\prime})\, \bar{\mathscr{D}}_{t'} K(t, t') = 0.$$

In particular we can require

$$\bar{\mathscr{D}}_{t'} K(t, t') = 0. \tag{3.23}$$

Moreover, from (3.22) and (3.17) it follows that the Green's function K with equal time arguments, i.e. $K(t, t) = \mathscr{K}$, is independent of time and governed by the reduced differential equation

$$(\mathscr{L}' + \nabla^{2\prime})\, \mathscr{K}(\boldsymbol{r}, z, \boldsymbol{r}', z') = \delta(\boldsymbol{r}-\boldsymbol{r}')\, \delta(z-z') \tag{3.24}$$

with the boundary conditions

$$\left(\frac{\partial}{\partial z'} + \frac{N^2}{g}\right) \mathscr{K} = 0 \quad \text{for} \quad z' = 0 \tag{3.25a}$$

$$\frac{\partial}{\partial z'} \mathscr{K} = 0 \quad \text{for} \quad z' = -H. \tag{3.25b}$$

Comparing (3.24) and (3.25*a*, *b*) with the definition of the Green's function S for the nonlinear steady state (3.12) we find that

$$S(\boldsymbol{r}, z, \boldsymbol{r}', z') = \mathscr{K}(\boldsymbol{r}, z, \boldsymbol{r}', z'), \tag{3.26}$$

i.e. the nonlinear stationary Green's function S appears as a special case of the quasi-nonlinear Green's function K. Now we can separate the stationary contribution to the response function ψ given by (3.20). Integrating the first term of (3.20) by parts and then using the relation (3.23) to perform the time integration we arrive at

$$\begin{aligned} \psi(\boldsymbol{r}, z, t) = -f^2 \int \mathrm{d}\boldsymbol{r}' (S(\boldsymbol{r}, z, \boldsymbol{r}', -H) - K(\boldsymbol{r}, z, t, \boldsymbol{r}', -H, 0))\, h(\boldsymbol{r}') \\ - f \int \mathrm{d}\boldsymbol{r}' \int_0^\infty \mathrm{d}t'\, G(\boldsymbol{r}, z, t, \boldsymbol{r}', -H, t')\, J(\psi(\boldsymbol{r}', -H, t'), h(\boldsymbol{r}')). \end{aligned} \tag{3.27}$$

The first term in the first integral is independent of time and equals the nonlinear stationary solution ψ^S, compare (3.11). Provided that the time-dependent terms tend to zero for large times the quasi-nonlinear approximation gives the correct nonlinear stationary limit.

In order to be more specific we confine ourselves to a homogeneous background flow

$$(u_0(\boldsymbol{r}, z, t), v_0(\boldsymbol{r}, z, t)) = (U_0(t), 0). \tag{3.28}$$

In this case the Green's function reads explicitly

$$G(\boldsymbol{r}, z, t, \boldsymbol{r}', z', t') = \theta(t-t')\, K(s, z, s', z')$$

with
$$K(\boldsymbol{s}, z, \boldsymbol{s}', z') = -(2\pi)^{-1} \sum_n F_n(z)\, F_n(z')\, K_0(|\boldsymbol{s}-\boldsymbol{s}'|/R_n). \tag{3.29}$$

Note that K depends on time only via the time-dependent radius vector

$$\boldsymbol{s} = \boldsymbol{r} - \boldsymbol{\omega}(t) \tag{3.30}$$

with
$$\boldsymbol{\omega}(t) = \int_0^t \mathrm{d}\tau (U_0(\tau), 0). \tag{3.31}$$

The F_n are the vertical eigenfunctions of the flat-bottom case, the R_n are the corresponding Rossby radii, and K_0 is a modified Bessel function, see Appendix A.

The linear approximation of the Green's function, L, defined by (3.3) follows in the limit $\boldsymbol{\omega}(t) \to 0$. This amounts to the formal replacement of $|\boldsymbol{s}-\boldsymbol{s}'|$ by $|\boldsymbol{r}-\boldsymbol{r}'|$ in K, i.e.

$$L(\boldsymbol{r}, z, t, \boldsymbol{r}', z', t') = \theta(t-t')\, K(\boldsymbol{r}, z, \boldsymbol{r}', z').$$

On the other hand, the Green's function S needed in the nonlinear stationary approximation follows as $S = K$ for $t = t'$.

Next we discuss the response scenario in the quasi-nonlinear approximation on the basis of (3.27) in more detail. As stated above, the first term of the first integral in (3.27) is independent of time and gives the stationary part of the response function, ψ^S. We anticipate that it describes an anticyclonic vortex trapped over the topographic feature h where the streamlines are following the contour lines of the bottom topography. Since the Green's function is peaked at $|\boldsymbol{s}-\boldsymbol{s}'| = 0$ it follows that the second part describes a cyclonic vortex which has exactly the same structure as ψ^S, apart from the sign, and which is shed downstream along the path $\boldsymbol{r} = \boldsymbol{\omega}(t)$. Thus, the cyclonic vortex leaves the isolated topographic feature provided that the flow $\boldsymbol{u}_0$ is non-oscillatory.

The second integral describes the interaction of the induced flow with the topography. As mentioned in §3.1, for small times the linear approximation applies and the response function ψ^L is a wave-type solution of the quasi-geostrophic vorticity equation. Examples of such waves are discussed in §5. If the second vortex moves downstream a smaller part of the associated currents can strike the topography so that the topographic waves are damped by vortex shedding.

To show this qualitatively for an isolated obstacle localized around $\boldsymbol{r} = 0$ we iterate the integral equation (3.27). Let $\psi^{(0)}$ be the integral

$$\psi^{(0)}(\boldsymbol{r}, t) = -f^2 \int \mathrm{d}\boldsymbol{r}'\, K(\boldsymbol{r}, -H, t, \boldsymbol{r}', -H, 0)\, h(\boldsymbol{r}').$$

We insert the inhomogeneous term, $\psi^{(0)}(\boldsymbol{r}, 0) - \psi^{(0)}(\boldsymbol{r}, t)$, as the zeroth approximation to ψ into the second integral. Since the streamlines of $\psi^{(0)}(\boldsymbol{r}, 0)$ follow the contour

lines of h, only $\psi^{(0)}(\boldsymbol{r}, t)$, which is centred at $\boldsymbol{r} = \boldsymbol{u}(t)$, contributes to the first iterate $\psi^{(1)}$. We can easily convince ourselves that since h is localized, $\psi^{(1)}$ must have the structure

$$\int_0^t \mathrm{d}t' \, K_0(t-t') \, \psi^{(0)}(t').$$

The asymptotic behaviour of the Bessel function, $K_0(x) \approx \mathrm{e}^{-x}/x^{\frac{1}{2}}$, implies that both functions under the integral are localized in regions where their arguments are small and diminish rapidly for large arguments. Thus, the two functions are non-zero at the opposite limits of the integration interval. Consequently the integral vanishes for large times and $\boldsymbol{r}$ confined to the vicinity of the obstacle and, therefore, the quasi-nonlinear approach equals in fact the steady-state solution for large times.

In summary the quasi-nonlinear approach gives a correct description of the limit cases both in the linear approach and the nonlinear stationary limit.

4. Response at infinitely long ridges

As first example we consider the simple case of infinitely long ridges stretching parallel to the y-axis, i.e.

$$h(\boldsymbol{r}) = h(x), \tag{4.1}$$

and a constant and homogeneous background flow U_0, i.e. $\boldsymbol{u}(t) = U_0 t$. Inserting (4.1) into (3.20) and using (3.29) and (A 22) we obtain from the first integral

$$\psi_0(x, z, t) = f^2 \int_{-a}^{a} \mathrm{d}x' \, h(x') \sum_n F_n(-H) \, F_n(z) \, \tfrac{1}{2} R_n [\exp(-|x-x'|/R_n)$$

$$-\exp(-|x-x'-U_0 t|/R_n)] = f^2 \sum_n F_n(-H) \, F_n(z) \, R_n^2 (\Pi_n(x) - \Pi(x-U_0 t)), \tag{4.2}$$

where

$$\Pi_n(x) = \int \mathrm{d}x' \frac{h(x')}{2R_n} \exp(-|x-x'|/R_n). \tag{4.3}$$

Since ψ_0 is independent of y it follows that $J(\psi_0, h)$ is zero. Solving the integral equation by iteration reveals that the second integral in (3.14) vanishes and hence ψ_0 is already the complete solution

$$\psi(x, z, t) = \psi_0(x, z, t). \tag{4.4}$$

The geostrophic currents follow as

$$u = U_0 - \frac{\psi_y}{f} = U_0, \tag{4.5}$$

and

$$v = \frac{\psi_x}{f} = f \sum_n F_n(z) \, F_n(-H) \, R_n^2 (\Pi_{nx}(x) - \Pi_{nx}(x-U_0 t)). \tag{4.6}$$

The associated density anomaly is

$$\frac{\Delta\rho}{\rho_0} = -\frac{\psi_z}{g} = f^2 \sum_n F_n(-H) \frac{\partial}{\partial z} F_n(z) \, R_n^2 (\Pi_n(x) - \Pi_n(x-U_0 t)). \tag{4.7}$$

The response consists of a stationary pattern trapped at the feature and a mirror image of that pattern moving downstream with the background current U_0. If the background flow were switched off at $t = T$, then stationary patterns would remain above the feature and at $x = U_0 T$ as well.

Topographic waves are not excited in this case. This follows from the fact that the topographically induced response ψ is parallel to f/H contours from the very beginning of the response scenario as a consequence of $J(\psi, h) = 0$. Excitation of topographic waves is only possible if the shape of the feature also depends on y.

Inserting (4.2) into (2.1) and (2.6a, b) reveals that (4.4)–(4.7) is the solution of the full nonlinear vorticity equation (2.10) with the boundary conditions (2.11a, b). This is because ψ is independent of y.

Owing to the simplicity of the solution it is easy to investigate how the shape of the ridge affects the response pattern. We consider three examples explicitly: a flat-topped ridge, a truncated cosine profile and a Gaussian-shaped profile.

(i) For a flat-topped ridge

$$h(\boldsymbol{r}) = \eta(\theta(x+a)-\theta(x-a)) = \eta\theta(a-|x|) \tag{4.8}$$

we find from (4.3)

$$\Pi_n(x) = h(x)+\eta\left[\operatorname{sgn}(x-a)\exp\left(-\frac{|x-a|}{R_n}\right)-\operatorname{sgn}(x+a)\exp\left(-\frac{|x+a|}{R_n}\right)\right]. \tag{4.9}$$

With the vertical eigenfunctions and eigenvalues (A 11), (A 12) and using the sum

$$\sum_n (-1)^n \cos n\alpha \frac{\mathrm{e}^{-n\beta}}{n} = -\tfrac{1}{2}\ln(2\mathrm{e}^{\beta}(\cosh\beta)+\cos\alpha)) \tag{4.10}$$

we obtain from (4.6) the closed-form expression

$$\begin{aligned} v(x,z,t) = \frac{\eta f}{2H_0}\Bigg\{ & R_0\left[\exp\left(-\frac{|x+a|}{R_0}\right)-\exp\left(-\frac{|x-a|}{R_0}\right)+\exp\left(-\frac{|x-U_0t-a|}{R_0}\right)\right. \\ & \left.-\exp\left(-\frac{|x-U_0t+a|}{R_0}\right)\right]-|x-a|+|x+a|-|x-Ut+a|+|x-Ut-a| \\ & +R_1\left(\ln\left[\frac{\cosh((x+a-U_0t)/R_1)+\cos(\pi z/H_0)}{\cosh((x-a-U_0t)/R_1)+\cos(\pi z/H_0)}\right]\right. \\ & \left.\left.-\ln\left[\frac{\cosh((x+a)/R_1)+\cos(\pi z/H_0)}{\cosh((x-a)/R_1)+\cos(\pi z/H_0)}\right]\right)\Bigg\}. \end{aligned} \tag{4.11}$$

Using the sum

$$\sum_n \frac{(-1)^n}{n}\sin(n\alpha)\,\mathrm{e}^{-n\beta} = -\arctan\left(\frac{\sin\alpha}{\mathrm{e}^{\beta}+\cos\alpha}\right)$$

we can also find a closed-form expression for the density anomaly

$$\begin{aligned} \frac{\Delta\rho}{\rho_0} = \frac{\eta}{H_0}\frac{R_1^2}{R_0^2}\Bigg\{ & \tfrac{1}{2}\pi^2\left(1+\frac{z}{H_0}\right)\left[\operatorname{sgn}(x-a)\left(\exp\left(-\frac{|x-a|}{R_0}\right)-1\right)\right. \\ & -\operatorname{sgn}(x+a)\left(\exp\left(-\frac{|x+a|}{R_0}\right)-1\right)+\operatorname{sgn}(x-U_0t+a)\left(\exp\left(-\frac{|x-U_0t+a|}{R_0}\right)-1\right) \\ & \left.-\operatorname{sgn}(x-U_0t-a)\left(\exp\left(-\frac{|x-U_0t-a|}{R_0}\right)-1\right)\right] \\ & +\operatorname{sgn}(x-a)\left[\tfrac{1}{2}\pi\frac{z}{H_0}-\arctan\left(\frac{\sin(\pi z/H_0)}{\exp(|x-a|/R_1)+\cos(\pi z/H_0)}\right)\right] \end{aligned}$$

$$-\operatorname{sgn}(x-a-U_0t)\left[\tfrac{1}{2}\pi\frac{z}{H_0}-\arctan\left(\frac{\sin(\pi z/H_0)}{\exp(|x-a-U_0t|/R_1)+\cos(\pi z/H_0)}\right)\right]$$

$$-\operatorname{sgn}(x+a)\left[\tfrac{1}{2}\pi\frac{z}{H_0}-\arctan\left(\frac{\sin(\pi z/H_0)}{\exp(|x+a|/R_1)+\cos(\pi z/H_0)}\right)\right]$$

$$+\operatorname{sgn}(x+a-U_0t)\left[\tfrac{1}{2}\pi\frac{z}{H_0}-\arctan\left(\frac{\sin(\pi z/H_0)}{\exp(|x+a-U_0t|/R_1)+\cos(\pi z/H_0)}\right)\right]\Bigg\}. \quad (4.12)$$

Choosing the numerical values of the parameters involved as $H_0 = 30$ m, $\eta = 3$ m, $a = 3$ km, $f = 1.2\times10^{-4}\ \mathrm{s}^{-1}$, $N = 10^{-2}\ \mathrm{s}^{-1}$, and $g = 9.81\ \mathrm{ms}^{-2}$ we obtain the vertical sections of density anomalies as shown in figure 1 (*a–d*). The plots display vertical sections for different values of the advection scales U_0t. In the initial phase, upwelling generated at the upstream side of the ridge and downwelling on the other side induce density changes at the edges of the ridge. Later the density anomalies move with U_0 and leave behind a positive density anomaly doming over the ridge while the negative density anomaly has been drifted away in the x-direction.

(ii) As second example we consider a cosine-shaped ridge

$$h(x) = \eta\cos\left(\frac{\pi}{2a}x\right)\theta(a-|x|). \quad (4.13)$$

From (4.3) it follows

$$\Pi_n(x) = \frac{1}{1+(\pi R_n/2a)^2}\left(h(x)+\frac{\eta\pi R_n}{2a}\left[\exp\left(-\frac{|x-a|}{R_n}\right)+\exp\left(-\frac{|x+a|}{R_n}\right)\right]\right). \quad (4.14)$$

Thus, similar to the top-hat case, (4.14) has the shape of the topographic feature (first term). In addition there are two exponential terms which smooth out the transition at the edges of the ridge, $x = \pm a$.

Inserting (4.14) in (4.2), (4.6), and (4.7) the complete solution can easily be found. As an example the resulting density anomaly for large U_0t is sketched in figure 1 (*e*).

(iii) As our third example we choose, as an infinitely differentiable shape, a Gaussian profile

$$h(x) = \eta\exp(-(x/a)^2). \quad (4.15)$$

For Π_n we obtain in this case

$$\Pi_n(x) = \tfrac{1}{4}h(x)\,a\pi^{\frac{1}{2}}\left\{\exp\left[\left(\frac{a}{2R_n}-\frac{x}{a}\right)^2\right]\operatorname{erfc}\left(\frac{a}{2R_n}-\frac{x}{a}\right)\right.$$

$$\left.+\exp\left[\left(\frac{a}{2R_n}+\frac{x}{a}\right)^2\right]\operatorname{erfc}\left(\frac{a}{2R_n}+\frac{x}{a}\right)\right\}, \quad (4.16)$$

where erfc (x) is the complementary error function, see Abramowitz & Stegun (1984). Inserting (4.15), (4.16) into (4.2), (4.6), and (4.7) gives the description of the response to the profile (4.15). In figure 1 (*f*) the resulting density anomaly is shown for large values of U_0t.

A comparison of the pattern shown in figure 1 (*a–f*) reveals that the structure of the response is not very much affected by the explicit shape of the ridges. Generally $\Pi_n(x)$ has the shape of the ridge profile $h(x)$ with some modifications controlled by the Rossby radius.

Since for large arguments erfc (x) approaches $\exp(-x^2)$ it follows from (4.16) that

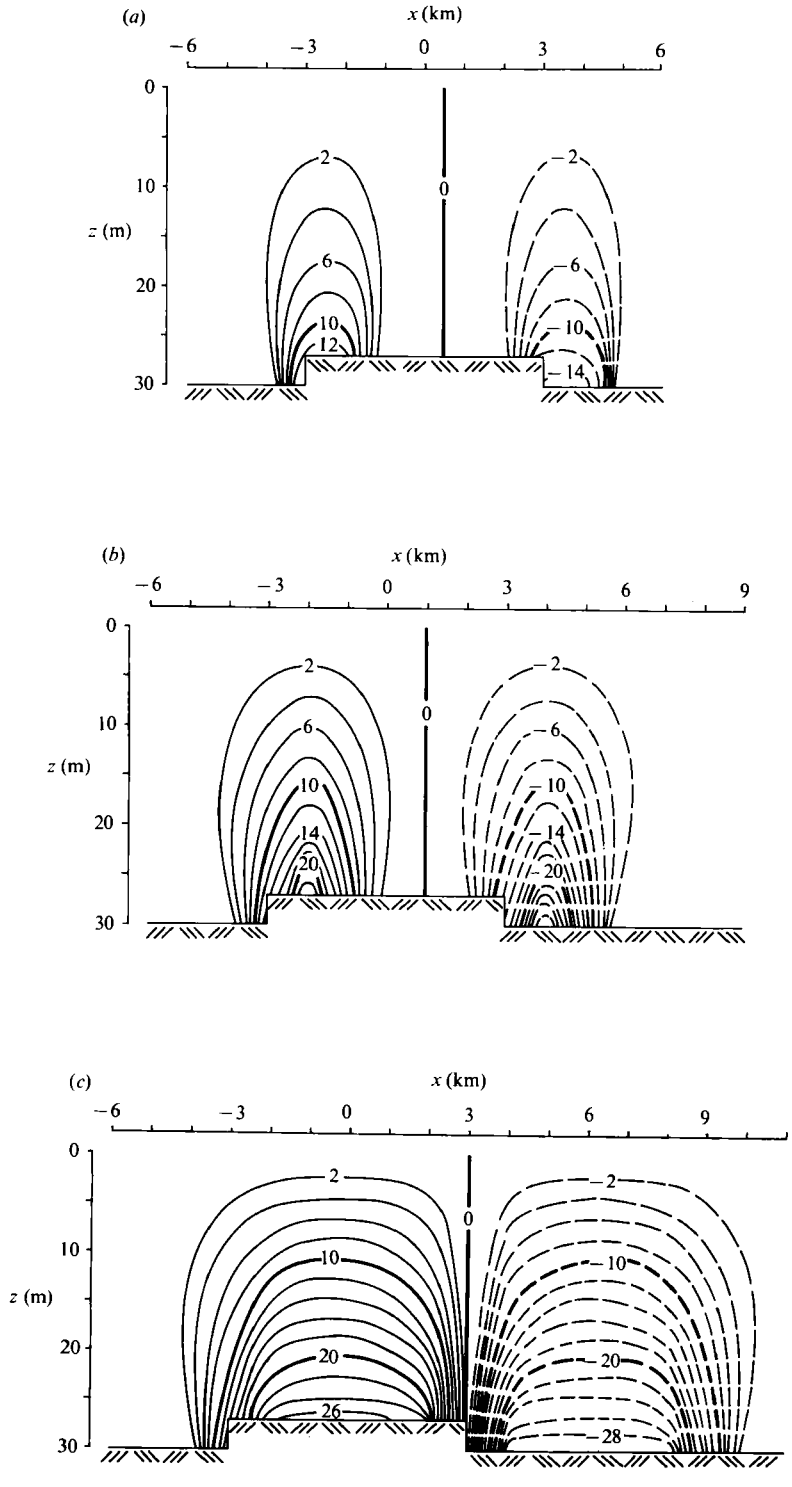

FIGURE 1 (*a–c*). For caption see facing page.

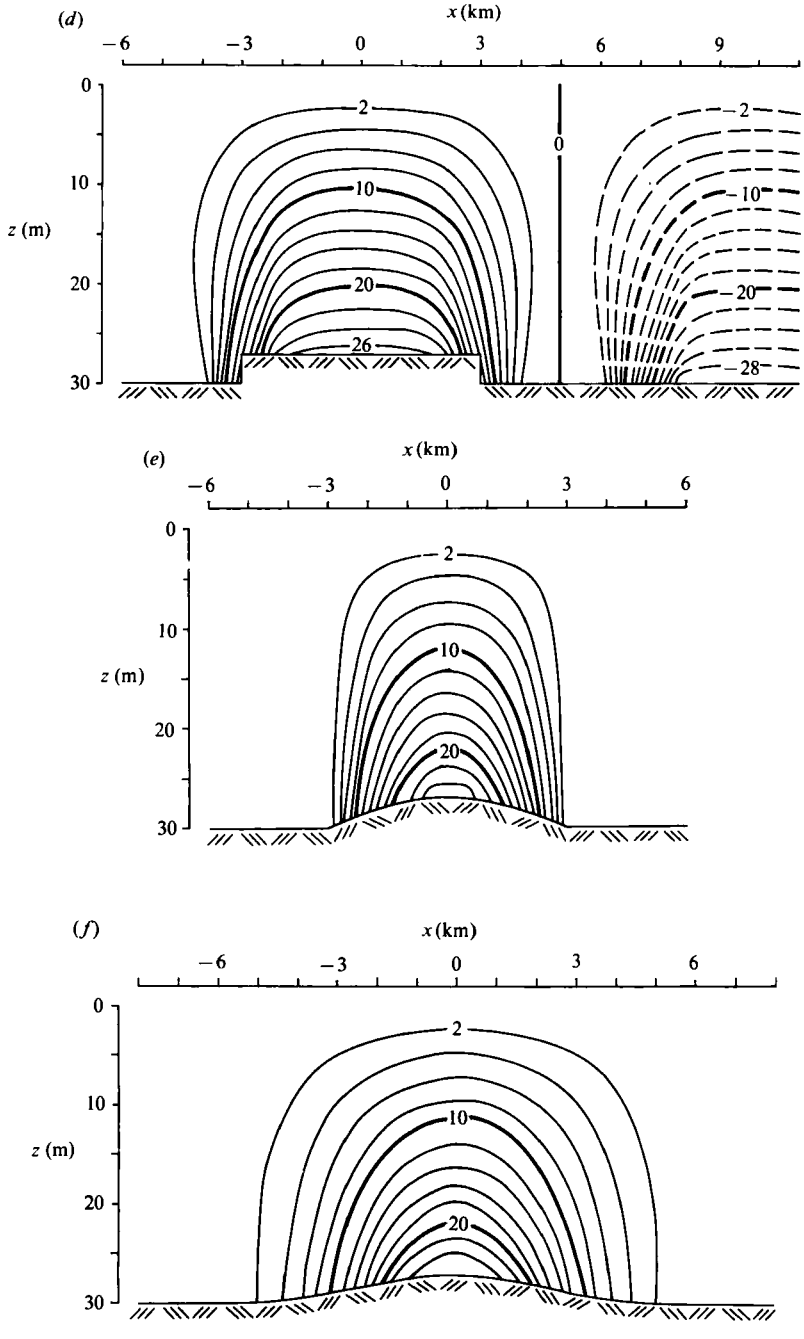

FIGURE 1. Plots of the topographically induced density anomaly in response to an upstream current flowing over a long ridge. The plots are for increasing values of the advection scale $U_0 t$ and the labels on the contours show values of $\Delta\rho/\rho_0 \times 10^6$. (*a*) $U_0 t = 1$ km: initially up- and downwelling at the up- and downstream edges of the ridge generate positive and negative density anomalies. (*b*) $U_0 t = 2$ km: later these patterns are moved downstream. (*c*) $U_0 t = 6$ km: if the positive anomaly arrives at the downstream edge the negative density anomaly generated earlier will be annihilated. (*d*) $U_0 t = 10$ km: finally a stationary, bell-shaped positive density anomaly remains, doming over the ridge, while a corresponding negative density anomaly has been shed. (*e*) density anomaly over a cosine profile in the final steady state. (*f*) as (*e*), but for a Gaussian-shaped profile.

Π_n converges to $h(x)$ for large values of the ratio a/R_n. In the cases of truncated profiles, (4.8) and (4.13), there are rectifying terms, see the exponentials in (4.9) and (4.14), which smooth out the response patterns at the edges of the ridges.

Finally we note that according to (4.2) the pressure is dominated by the barotropic mode while this mode plays a minor part in the density anomalies.

Since in nature ridges are always of finite length we have to expect that topographic waves, excited at the ends of the ridges would emerge. Thus for finite-length ridges our solutions apply only as long as the topographic waves have not reached the area considered. Moreover, a background flow of finite width would also force topographic waves. Such cases are, for example, studied in the papers of Willmott (1984) and Killworth (1989). The properties of topographic waves strongly affected by the shape of the ridges and the solutions show very complex structures, see e.g. figures 10 and 11 in the paper of Killworth (1989). Such problems require numerical solutions of the dynamic equations.

The idealized example considered in the present paper appears to be one of the rare cases where analytical solutions of the nonlinear vorticity equation can be obtained. In the case of a top-hat ridge it is even possible to derive closed-form expressions for the geostrophic current and the density anomaly.

5. Response at an axisymmetric obstable – linear case

In this section we analyse the topographically forced response to axisymmetrical obstacles. For simplicity we choose a right-circular cylinder

$$h(\boldsymbol{r}) = \eta\theta(a-r). \tag{5.1}$$

We consider a homogeneous time-dependent upstream flow $u_0(t)$ suddenly switched on at $t = 0$. In the initial phase, $u(t) \ll a$, we can expect a linear response governed by (3.6). Introducing cylindrical polar coordinates (3.6) can be rewritten as

$$\psi^L(r,\varphi,z,t) = -f^2 \int_0^\infty \mathrm{d}r'\, r' \int_0^{2\pi} \frac{\mathrm{d}\varphi'}{2\pi} \int_0^t \mathrm{d}t' \sum_{m=-\infty}^{+\infty} \mathrm{e}^{\mathrm{i}m(\varphi-\varphi')} L_m(\boldsymbol{r}, z, \boldsymbol{r}', -H_0)$$
$$\times \left\{ u_0(t')\cos\varphi' - \frac{1}{fr'} \frac{\partial}{\partial\varphi'} \psi(r', \varphi', -H, t') \right\} \frac{\partial}{\partial r'} h(\boldsymbol{r}'). \tag{5.2}$$

Since $(\partial/\partial r')\, h(\boldsymbol{r}') = -\eta\delta(a-r')$ the r'-integration is trivial.

The time integral is of convolution type. Thus, by Fourier transformation

$$A(t) = \int_{-\infty}^{+\infty} \frac{\mathrm{d}\omega}{2\pi} \mathrm{e}^{-\mathrm{i}\omega t} A(\omega), \tag{5.3}$$

and expansion of ψ^L into a Fourier series in φ,

$$\psi^L(r,\varphi) = \sum \frac{\mathrm{e}^{\mathrm{i}m\varphi}}{2\pi} \psi_m^L(r), \tag{5.4}$$

(5.2) can be converted into an algebraic equation

$$\psi_m^L(r,z,\omega) = \frac{i}{\omega+\mathrm{i}\epsilon} \eta f L_m(r,z,a,-H_0)\,(\pi a u_0(\omega)\,(\delta_{m1}+\delta_{m-1}) - im\psi_m^L(a,-H_0,\omega)). \tag{5.5}$$

Here the orthogonality of the functions $\mathrm{e}^{\mathrm{i}m\varphi}$ has been used. We denote the Fourier

transforms with the same symbol as the original function. Both quantities can be distinguished by their arguments. The positive infinitesimal ϵ occurring in (5.5) prescribes how to avoid the singularities of $\psi_m^L(\omega)$ when performing the inverse Fourier transformation.

The solution of (5.5) is

$$\psi_m^L(r,z,\omega) = \frac{\mathrm{i}u_0(\omega)}{\omega+\mathrm{i}\epsilon+m\gamma_m}\pi a\eta f L_m(r,z,a,-H_0)(\delta_{m1}+\delta_{m-1}), \tag{5.6}$$

where the abbreviation γ_m stands for

$$\gamma_m = -\eta f L_m(a,-H_0,a,-H_0). \tag{5.7}$$

The sum over m can easily be performed and we obtain after inverse Fourier transform

$$\psi(r,\varphi,z,t) = \Gamma(r,z)\,Q(\varphi,t), \tag{5.8}$$

where

$$\Gamma(r,z) = f^2\eta a L_1(r,z,a,-H_0) \tag{5.9}$$

and

$$Q(\varphi,t) = \int_0^t \mathrm{d}t'\,u_0(t-t')\cos(\varphi+f_{\mathrm{top}}t'). \tag{5.10}$$

This is the solution of the linear vorticity equation (3.6) for a homogeneous time-dependent current u_0 flowing over a right-circular cylinder. We note that a 'topographic frequency' $f_{\mathrm{top}} = \gamma_1$ has emerged which is defined by (5.7) for $m = 1$. Inserting the Green's function according to (A 18) we find

$$f_{\mathrm{top}} = \gamma_1 = f\eta\left(g_{10}(a,a)F_0^2 + \sum_{n=1}^{\infty} F_n(-H_0)F_n(-H_0+\eta)\,g_{1n}(a,a)\right). \tag{5.11a}$$

It is a consequence of the axisymmetry of the example considered that only a topographic frequency with $m = \pm 1$ occurs.

In (5.11 *a*) we have written one of the vertical eigenfunctions F_n with the argument $-H_0+\eta$ in order to avoid a singularity. Here we can argue as follows. In the Green's function $L_m(r,z,a,-H_0)$ we have put $r' = a$. If r also approaches the edge of the cylinder, $r \to a$, then the step functions in g_{nm} imply that the edges are approached from $a^+ = a+\epsilon$ and $a^- = a-\epsilon$ respectively. In the former case the depth is H_0 while in the latter case the depth is $H_0-\eta$.

Using the vertical eigenfunctions (A 11) and (A 12) and assuming $a \gg R_1$ we find approximately

$$f_{\mathrm{top}} \approx \frac{f\eta}{2H_0}\left[1-\frac{2R_1}{a}\ln\left(2-2\cos\left[\frac{\pi\eta}{H_0}\right]\right)\right]. \tag{5.11b}$$

We note that f_{top} is independent of u_0. The first term in (5.11 *b*) is the frequency of a double Kelvin wave in a homogeneous fluid proportional to half the inertial frequency reduced by the factor η/H_0. The second term is due to the effects of stratification through the baroclinic Rossby radius and depends on the horizontal scale of the topographic feature.

In figure 2 (*a*) the topographic frequency is depicted versus h/H_0 for various ratios R_1/a. The barotropic part dominates for $R_1/a \ll 1$, i.e. for weak stratification or obstacles with large horizontal scale. The baroclinic contribution to f_{top} is most significant for small topographic heights, i.e. $h/H_0 \ll 1$, and not too small ratios R_1/a. This is also demonstrated in figure 2 (*b*) where the relative shift of the topographic frequency due to stratification is shown versus R_1/a.

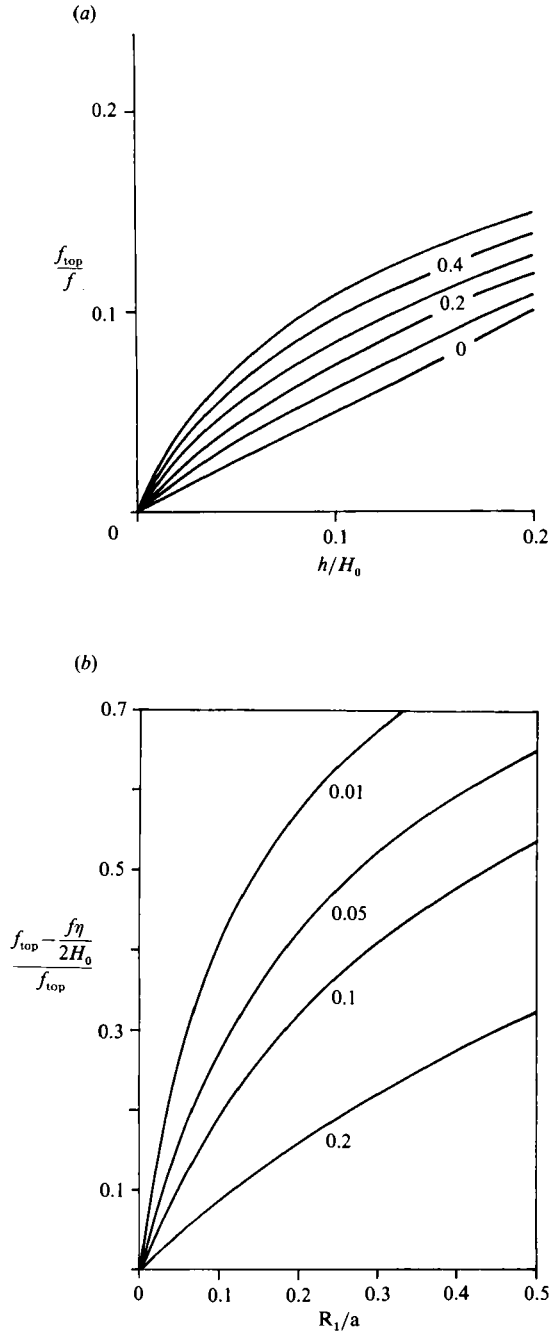

FIGURE 2. (*a*) The topographic frequency f_{top} as function of the obstacle height h/H_0 for various ratios of the first baroclinic Rossby radius to the cylinder radius, R_1/a. The straight line depicts the barotropic case, while baroclinic effects become important especially for strong stratification or a small radius of the cylinder. (*b*) The relative shift of the topographic frequency due to stratification. Baroclinic effects become important especially for small obstacles.

In order to study the influence of friction we may introduce simple linear dissipation. This can be achieved by the formal replacement of $\partial/\partial t$ by $\partial/\partial t+\nu$ in the quasi-geostrophic equations. This amounts to a multiplication of the Green's function L by a factor $e^{-\nu(t-t')}$ and we obtain instead of (5.10)

$$Q(\varphi, t) = \int_0^t dt'\, u_0(t-t')\, e^{-\nu t'} \cos(\varphi + f_{\text{top}} t'). \tag{5.12}$$

The solution (5.9), (5.10) describes a topographically trapped wave moving clockwise round the obstacle. This can be seen most explicitly in the case of a pulse-like forcing, where the upstream current is switched on and then off after a short time interval Δt

$$u_0(t) = u_0^*(\theta(t)-\theta(t-\Delta t)) \approx u_0^*\, \delta(t)\, \Delta t.$$

Then from (5.12) it follows that

$$\psi(r, \varphi, z, t) = u_0^*\, \Delta t f^2 \eta a \cos(\varphi + t f_{\text{top}}) L_1(r, z, a, -H_0). \tag{5.13}$$

Thus, a pulse excites a free topographically trapped wave cycling clockwise round the cylinder with angular frequency $-f_{\text{top}}$. The wavelength equals one circumference of the cylinder. If no damping is included the motion continues with constant wave amplitude. However, since the amplitude is proportional to Δt, which is small by definition, the resulting signals are weak.

For a forcing switched on at $t = 0$ and being constant thereafter, $u_0(t) = u_0^*\, \theta(t)$, we find

$$Q(\varphi, t) = \frac{u_0^*}{f_{\text{top}}} [\sin(\varphi + t f_{\text{top}}) - \sin\varphi]. \tag{5.14a}$$

With friction it follows that

$$Q(\varphi, t) = \frac{u_0^*}{\nu^2 + f_{\text{top}}^2} [f_{\text{top}}(e^{-\nu t} \sin(\varphi + f_{\text{top}} t) - \sin\varphi) - \nu(e^{-\nu t} \cos(\varphi + f_{\text{top}} t) - \cos\varphi)]. \tag{5.14b}$$

If the baroclinic terms are dropped this result equals the barotropic solution given by Johnson (1984).

In order to illustrate the solutions we have sketched the wave patterns by means of the density anomalies $\Delta\rho/\rho_0$:

$$\frac{\Delta\rho}{\rho_0} = -\frac{1}{g}\psi_z(r, \varphi, z, t) = -\frac{1}{g} Q(\varphi, t) \frac{\partial}{\partial z} \Gamma(r, z).$$

The parameters involved are chosen as $H_0 = 30$ m, $\eta = 3$ m, $a = 3$ km, $N = 10^{-2}\ \text{s}^{-1}$. This choice applys to shallow seas as, for example, the Arkona basin in the Baltic Sea. The numerical value of the topographical frequency becomes $f_{\text{top}} = 9.7 \times 10^{-6}\ \text{s}^{-1}$.

The density anomalies in response to a switched on forcing as given by (5.15) are shown in figure 3, where four snapshots of $\Delta\rho_0/\rho$ at $z = -25$ m are plotted. The response pattern consists of positive and negative density anomalies which in turn correspond to up- and downwelling, forming a clockwise rotating 'butterfly-pattern'. The motion of the pattern can be characterized by the angle, $\varphi(t)$, of the symmetry line $Q(\varphi(t), t) = 0$. From (5.14a) it follows that

$$\varphi(t) = \tfrac{1}{2}\pi - \tfrac{1}{2} f_{\text{top}}\, t,$$

i.e. the pattern rotates with the constant rate $-\frac{1}{2}f_{\text{top}}$. After rotation by almost 180°,

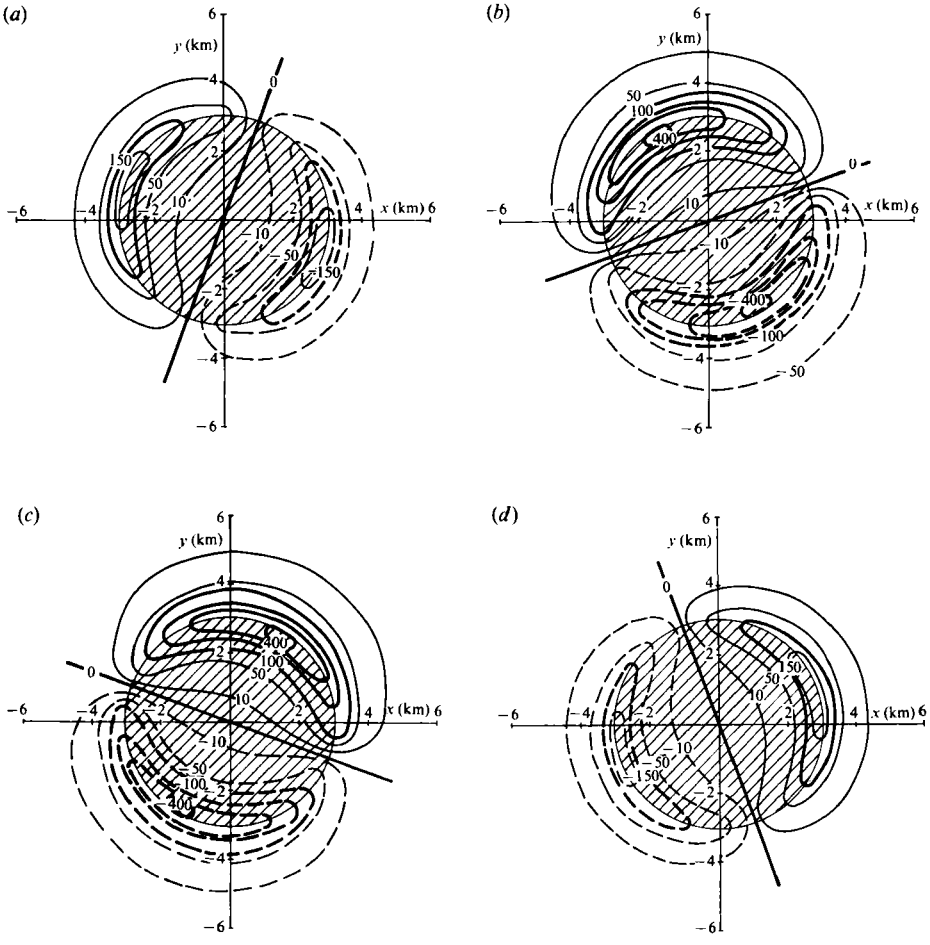

FIGURE 3. Four snapshots of density anomalies as produced by a topographically trapped wave in response to an upstream flow suddenly switched on at $t = 0$ and being constant thereafter. A butterfly-shaped pattern is generated which moves clockwise round the obstacle. Anomalies at a depth of 25 m are shown, the numerical values of the involved parameters are given in the text. (*a*) $t = 10^5$ s, (*b*) $t = 3 \times 10^5$ s, (*c*) $t = 5 \times 10^5$ s, (*d*) $t = 7 \times 10^5$ s. The labels on the contours are $\Delta\rho/\rho_0 \times 10^6$.

the up- and downwelling 'wings' approach the down- and upwelling centres up- and downstream of the obstacle and the pattern vanishes temporarily, and then the whole scenario starts again. If $f_{\text{top}}t$ equals integer multiples of 2π the pattern vanishes identically and hence the symmetry line is not well defined. These are the moments where the angle $\varphi(t)$ jumps from $\frac{1}{2}\pi$ to $-\frac{1}{2}\pi$ as sketched in figure 4.

If friction is taken into account the motion changes drastically. The angle of the symmetry line, $Q = 0$, follows from (4.14*b*) as

$$\varphi = \arctan\left(\frac{\alpha(1-\mathrm{e}^{-\alpha\tau}\cos\tau)+\mathrm{e}^{-\alpha\tau}\sin\tau}{1-\mathrm{e}^{-\alpha\tau}\cos\tau-\alpha\,\mathrm{e}^{-\alpha\tau}\sin\tau}\right) \tag{5.15a}$$

with $\alpha = \nu/f_{\text{top}}$ and $\tau = f_{\text{top}}t$. For large times a steady state establishes where the corresponding angle, φ_∞, is given by

$$\varphi_\infty = \arctan\alpha.$$

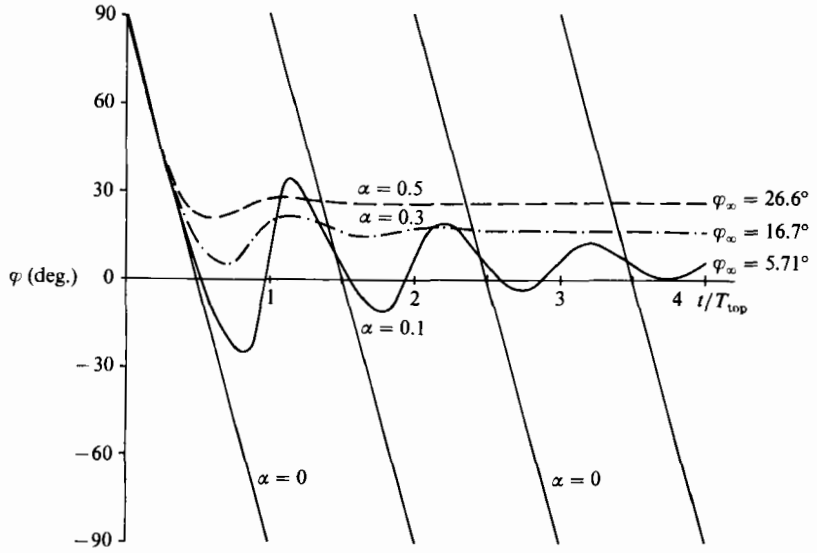

FIGURE 4. Angle of the symmetry line of the double vortex versus time for different damping rates, $\alpha = \nu/f_{\text{top}}$. T_{top} is the period given by $2\pi/f_{\text{top}}$. In the inviscid case, $\alpha = 0$, the pattern rotates from 90° to −90°, vanishes momentarily and starts again. Note that for $t = nT_{\text{top}}$ ($n = 1, 2, 3, \ldots$) the symmetry line is not defined because the pattern vanishes identically. Thus the angle seemingly jumps from −90° to 90°. For non-zero α the angle describes a pattern that oscillates while approaching a stationary state.

Thus the final orientation of the pattern is determined by the ratio of damping rate to topographic frequency. The time behaviour of $\varphi(t)$ is depicted in figure 4 for different damping rates α. The angular velocity, i.e. the phase speed of the topographic wave, follows from (5.15*a*) as

$$\frac{\partial \varphi}{\partial t} = -\tfrac{1}{2} f_{\text{top}} \frac{\mathrm{e}^{-\alpha\tau} - \cos\tau + \alpha \sin\tau}{\cosh(\alpha\tau) - \cos\tau}. \tag{5.15b}$$

Initially the patterns rotate with angular frequencies close to $-\frac{1}{2}f_{\text{top}}$. Later the motion decelerates and the patterns oscillate around the final position while approaching the steady state.

Since the validity of the linear approximation is restricted to times smaller than the advection time T_{a}, the inviscid solution applies only to the starting phase, $t \ll T_{\text{a}}$. In the viscous case (5.14*b*) is a consistent solution for strong damping rates, i.e. $\nu T_{\text{a}} \gg 1$.

Next we consider the response to an oscillatory background flow,

$$u_0(t) = u_0^* \theta(t) \sin \omega_0 t.$$

From (5.10) we obtain

$$Q(\varphi, t) = \frac{u_0^* \omega_0}{\omega_0^2 - f_{\text{top}}^2} \left(\cos(\varphi + t f_{\text{top}}) - \cos\varphi \cos\omega_0 t + \frac{f_{\text{top}}}{\omega_0} \sin\varphi \sin\omega_0 t \right). \tag{5.16}$$

In particular in the case of resonance, $\omega_0 = f_{\text{top}}$, this expression degenerates to

$$Q(\varphi, t) = \frac{u_0^*}{2 f_{\text{top}}} (t f_{\text{top}} \sin(\varphi + t f_{\text{top}}) - \sin\varphi \sin t f_{\text{top}}). \tag{5.17}$$

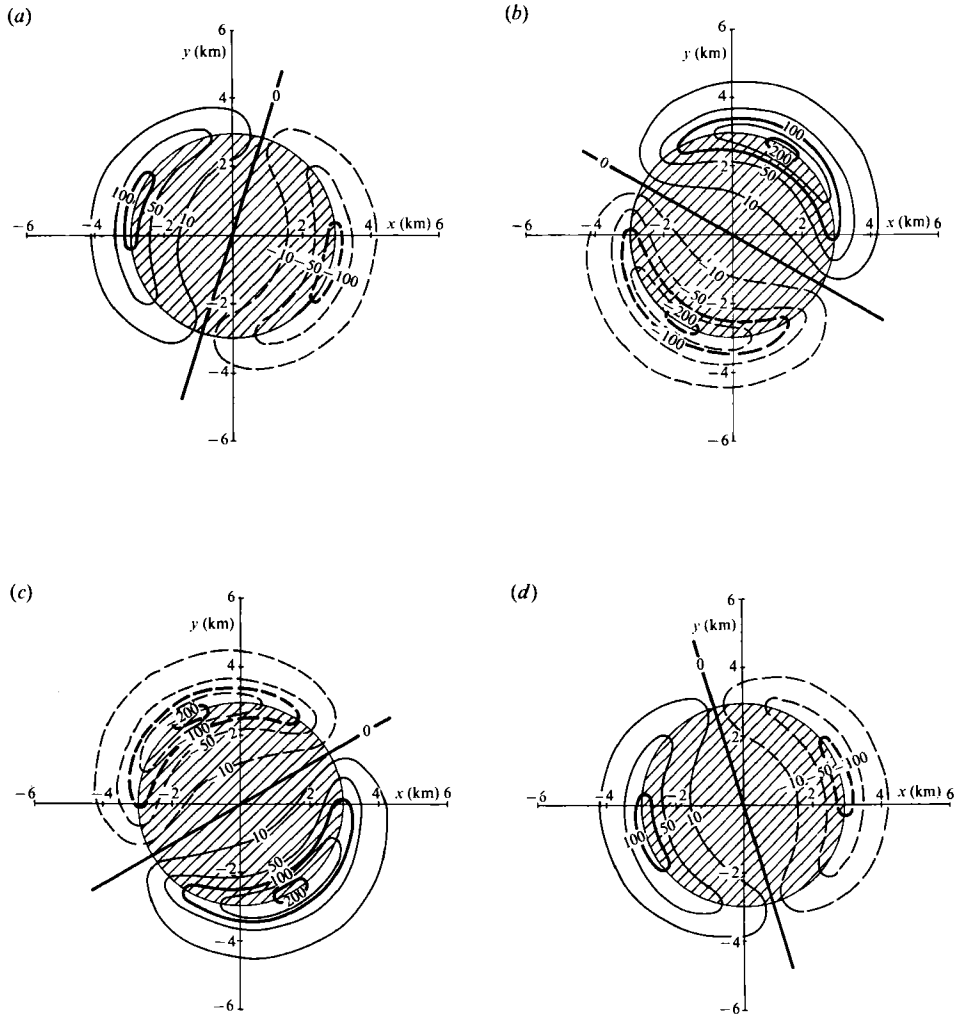

FIGURE 5. As figure 3, but for an oscillatory upstream flow alternating with a frequency $\omega_0 = 2f_{\text{top}}$. (*a*) $t = 10^5$ s, (*b*) $t = 3\times10^5$ s, (*c*) $t = 5\times10^5$ 2, (*d*) $t = 7\times10^5$ s.

The response patterns are displayed in terms of density anomalies in figure 5 for $\omega_0 = 2f_{\text{top}}$ and in figure 6 for $\omega_0 = f_{\text{top}}$. The parameters have been chosen as in figure 3.

The rotation rate of the symmetry line of the pattern, $Q = 0$, follows as

$$\frac{\partial\varphi}{\partial t} = -f_{\text{top}}\beta\left(\frac{4\beta+(1-\beta)^2\cos(1+\beta)\tau-(1+\beta)^2\cos(1-\beta)\tau}{4\beta^2-2\beta(1+\beta)\cos(1-\beta)\tau+2\beta(1-\beta)\cos(1+\beta)\tau+2(1-\beta^2)\sin^2\beta\tau)}\right), \tag{5.18}$$

where β is the ratio of the forcing frequency ω_0 to the topographical frequency, i.e. $\beta = \omega_0/f_{\text{top}}$, and $\tau = f_{\text{top}}t$. In figure 7 the angular velocity is shown for some rational values of β. Obviously the rate of rotation changes rapidly in time and thus the inviscid response to an oscillatory forcing appears to be rather complex. For irrational values of β the motion can be even more irregular. The small vertical bars in figure 7 indicate the moments where $\varphi(t)$ is not well defined because Q vanishes identically.

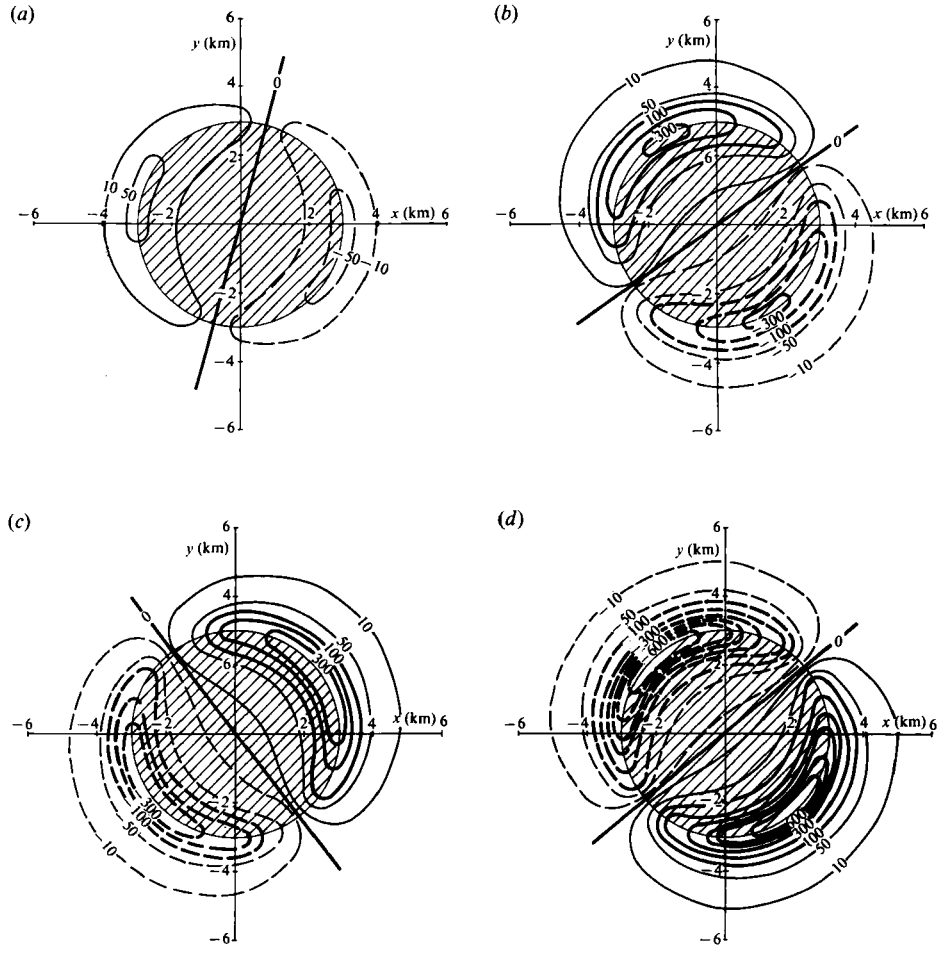

FIGURE 6. As figure 3, but for an oscillatory upstream flow alternating with the topographic frequency $\omega_0 = f_{\text{top}}$. In the resonance case the pattern rotates round the obstacle with an amplitude increasing linearly with time. (*a*) $t = 10^5$ s, (*b*) $t = 3 \times 10^5$ s, (*c*) $t = 5 \times 10^5$ s, (*d*) $t = 7 \times 10^5$ s.

In the case of resonance, $\beta = 1$, we find in particular

$$\frac{\partial \varphi}{\partial t} = -f_{\text{top}} \frac{\tau^2 - \sin^2 \tau}{\tau^2 - \sin^2 \tau + 2\tau \cos \tau \sin \tau}, \tag{5.19}$$

i.e. with increasing time the rotation rate tends to $-f_{\text{top}}$.

In order to check the range of validity of these results we need an advection timescale which is not well defined in the case of oscillatory forcing. However, we can define an advection scale, L_{a}, which measures the distance a fluid element can be advected by the background flow before u_0 changes its direction,

$$L_{\text{a}} = u_0^* \int_0^{T_0/2} \mathrm{d}t \sin \omega_0 t = \frac{u_0^* T_0}{\pi},$$

with $\omega_0 = 2\pi/T_0$. Then the linear approximation applies for $2A \gg L_{\text{a}}$. Thus, for our choice of parameters ($u_0^* = 5$ cm s^{-1}, $A = 3000$ m) the linear approximation is not well justified for an oscillatory flow with $\omega_0 \leqslant f_{\text{top}}$. Since, however, the range of

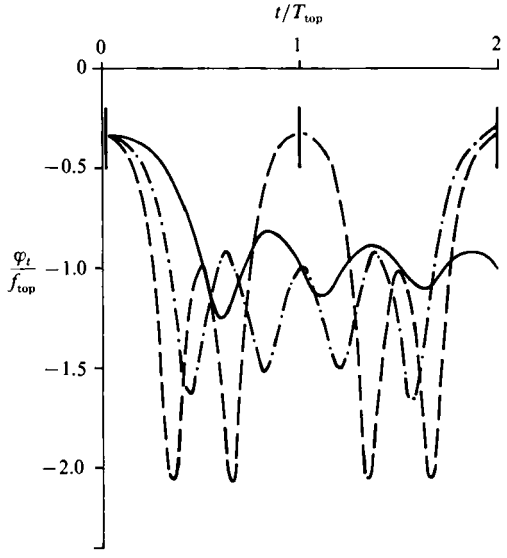

FIGURE 7. Angular velocity of the pattern in response to an oscillatory forcing relative to the topographical frequency: $\omega_0 = f_{top}$ (solid line), $\omega_0 = 1.5 f_{top}$ (dashed line), $\omega_0 = 2 f_{top}$ (dot-dashed line).

validity can be extended by reducing u_0^*, figures 5 and 6 give a correct visualization of the response pattern. Only the amplitude of the signals would be smaller for a reduced background velocity. In summary topographic waves forced by an oscillatory background flow with not too large an amplitude and not too small a frequency can be described in the framework of a linear theory.

6. Response at an axisymmetric obstacle – quasi-nonlinear case

Let us again consider a constant, homogeneous upstream current switched on at $t = 0$ and flowing over a cylindric obstacle as given by (5.1). After times exceeding the advection time, $T_a = 2a/U_0$, the advection of the topographically forced pattern by the upstream flow U_0 has to be taken into account. This can be accomplished by the quasi-nonlinear approximation where the response is described by (3.27). For a right-circular cylinder (5.1), we may rewrite (3.27) in plane polar coordinates as

$$\psi(r,\varphi,z,t) = -f^2\eta \int_0^{2\pi} \mathrm{d}\varphi' \int_0^a \mathrm{d}r'\, r'[K(\boldsymbol{r},z,\boldsymbol{r}',-H_0) - K(\boldsymbol{s},z,\boldsymbol{r}',-H_0)]$$
$$+ f\eta \int_0^{2\pi} \mathrm{d}\varphi' \int_0^{\infty} \mathrm{d}r'\, \delta(a-r') \int_0^t \mathrm{d}t'\, K(\boldsymbol{s},z,\boldsymbol{s}',-H_0) \frac{\partial}{\partial\varphi'} \psi(a,\varphi',-H,t') \quad (6.1)$$

where the vector $\boldsymbol{s}$ is defined as

$$s = s(t) = ((x-\alpha(t))^2 + y^2)^{\frac{1}{2}},$$

with components

$$s_x = x - \alpha(t) = s(t)\cos\Phi(t),$$
$$s_y = y = s(t)\sin\Phi(t).$$

With the aid of the Fourier series (A 18) the integrals in the first term of (6.1) can be evaluated explicitly:

$$\int_0^{2\pi}\frac{\mathrm{d}\varphi'}{2\pi}\int_0^a \mathrm{d}r'\,r'K_0\left(\frac{|\boldsymbol{r}-\boldsymbol{r}'|}{R_n}\right)=\int_0^a \mathrm{d}r'\,r'g_{01}(r,r')$$

$$=R_n\left(\theta(r-a)\,aK_0\left(\frac{r}{R_n}\right)I_1\left(\frac{a}{R_n}\right)+\theta(a-r)\left[R_n-aI_0\left(\frac{r}{R_n}\right)K_1\left(\frac{a}{R_n}\right)\right]\right), \quad (6.2)$$

where the standard integrals $\int \mathrm{d}x\,xK_0(x) = -xK_1(x)$, and $\int \mathrm{d}x\,xI_0(x) = xI_1(x)$ have been used. The second K_0-function in the first integral in (6.1) gives the same expression as (6.2), except that r has to be replaced by s.

Thus, with the notation

$$\Psi(r,z)=f^2\eta\sum_n F_n(-H)\,F_n(z)\,R_n\left(\theta(r-a)\,aK_0\left(\frac{r}{R_n}\right)I_1\left(\frac{a}{R_n}\right)\right.$$

$$\left.+\theta(a-r)\left[R_n-aI_0\left(\frac{r}{R_n}\right)K_1\left(\frac{a}{R_n}\right)\right]\right) \quad (6.3)$$

we can rewrite (6.1) as

$$\psi(r,\varphi,z,t)=\Psi(r,z)-\Psi(s,z)+f\eta\int_0^t \mathrm{d}t'\int_0^{2\pi}\mathrm{d}\varphi'\,\psi(a,\varphi',-H,t')\frac{\partial}{\partial\varphi'}K(\boldsymbol{s},z,\boldsymbol{s}',-H_0)|_{s'=a}. \quad (6.4)$$

As outlined in §3, the first term on the right-hand side of (6.4) is the steady solution which describes an anticyclonic vortex around the obstacle as already discussed by Hogg (1973) and Huppert (1975). The second term, which depends on t and φ through s, describes a cyclonic vortex shed downstream along the x-axis, moving with the background velocity u_0. The third term mirrors the interaction of the topographically induced current with the topographic feature. According to the previous section this mechanism is responsible for the generation of topographic waves.

We have solved the integro-differential equation (6.4) numerically. The numerical scheme is described in Appendix B. The results are depicted in figures 8 and 9, where the development of the solution is shown for two examples of non-oscillatory upstream flows. The numerical values of the parameters involved are the same as in the preceeding section. For a small upstream velocity, $u_0 = 1$ cm/s, the response is shown in figure 8. The pattern closely resembles that of a topographic wave shown in figure 3. If the upstream flow is enhanced by one order of magnitude, $u_0 =$ 10 cm/s, then the processes of vortex shedding dominate the response, as is visible in figure 9. Owing to the topographic waves in the initial phase the path of the shed cyclonic vortex has been shifted towards the negative y-axis. Further enhancement of the upstream flow decreases the role played by the topographic waves and the cyclonic vortex will move downstream with its centre along the x-axis. In those cases the interaction term in (6.4) contributes very little and the response is practically described by the first two terms of (6.4).

We note that Johnson (1984) has given a formula for the 'fast case', see (2.9) in this paper, which corresponds to (6.4). However, the integral term has been dropped and only the barotropic case with a rigid-lid condition for Green's function at the sea surface was considered. This is equivalent to using only the barotropic mode, $n = 0$, in (6.3) and taking the limit case $R_0 \to \infty$. From the behaviour of the Bessel function

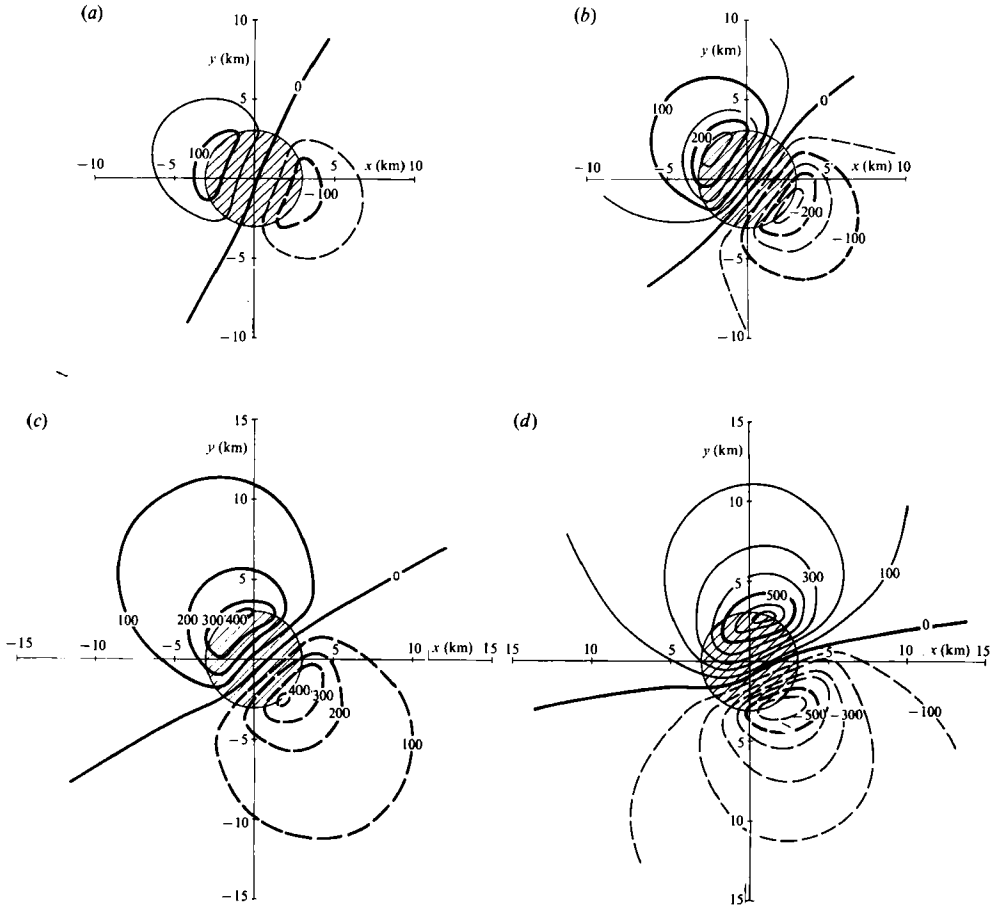

FIGURE 8. Plots of the topographically induced response of an upstream flow, switched on at $t = 0$ and being constant thereafter, in the framework of a quasi-nonlinear approximation scheme. The labels on the contours show values of $\psi \times 10^5$ ($m^2\ s^{-2}$). The changes in the pressure field are shown at 25 m depth for a small upstream velocity, $u_0 = 1$ cm/s. In this case the advection time is large and, consequently, the response pattern resembles that of the linear topographic wave displayed in figure 3. (*a*) $t = 5 \times 10^4$ s, (*b*) $t = 10^5$ s, (*c*) $t = 1.5 \times 10^5$ s, (*d*) $t = 2.5 \times 10^5$ s.

K_0 and I_0 for small arguments we find that the solution diverges logarithmically for an infinite barotropic Rossby radius. Thus, a proper choice of the sea-surface boundary condition, e.g. (3.19*a*), is of importance.

It is worth comparing our results with the numerical solutions of the full nonlinear Boussinesq equations as given in H & B. We start with the slow case (S), where the advection time is about 46 days and a linear response scenario can be expected. Actually, figure 8 of H & B reveals that a butterfly structure rotates clockwise round the obstacle. The maximum density anomaly is trapped near the steepest slope of the bottom profile and has a range of the order of the baroclinic Rossby radius, which is about 13 km for the parameters used in H & B. Within this butterfly structure shown in figure 8 in H & B the area of maximum density perturbation seems to rotate faster than the outer areas. We observe such behaviour neither in the linear approximation displayed in figure 3 nor in the quasi-nonlinear approximation for small background velocities as in figure 8. However, the analysis of a smoother obstacle given by a

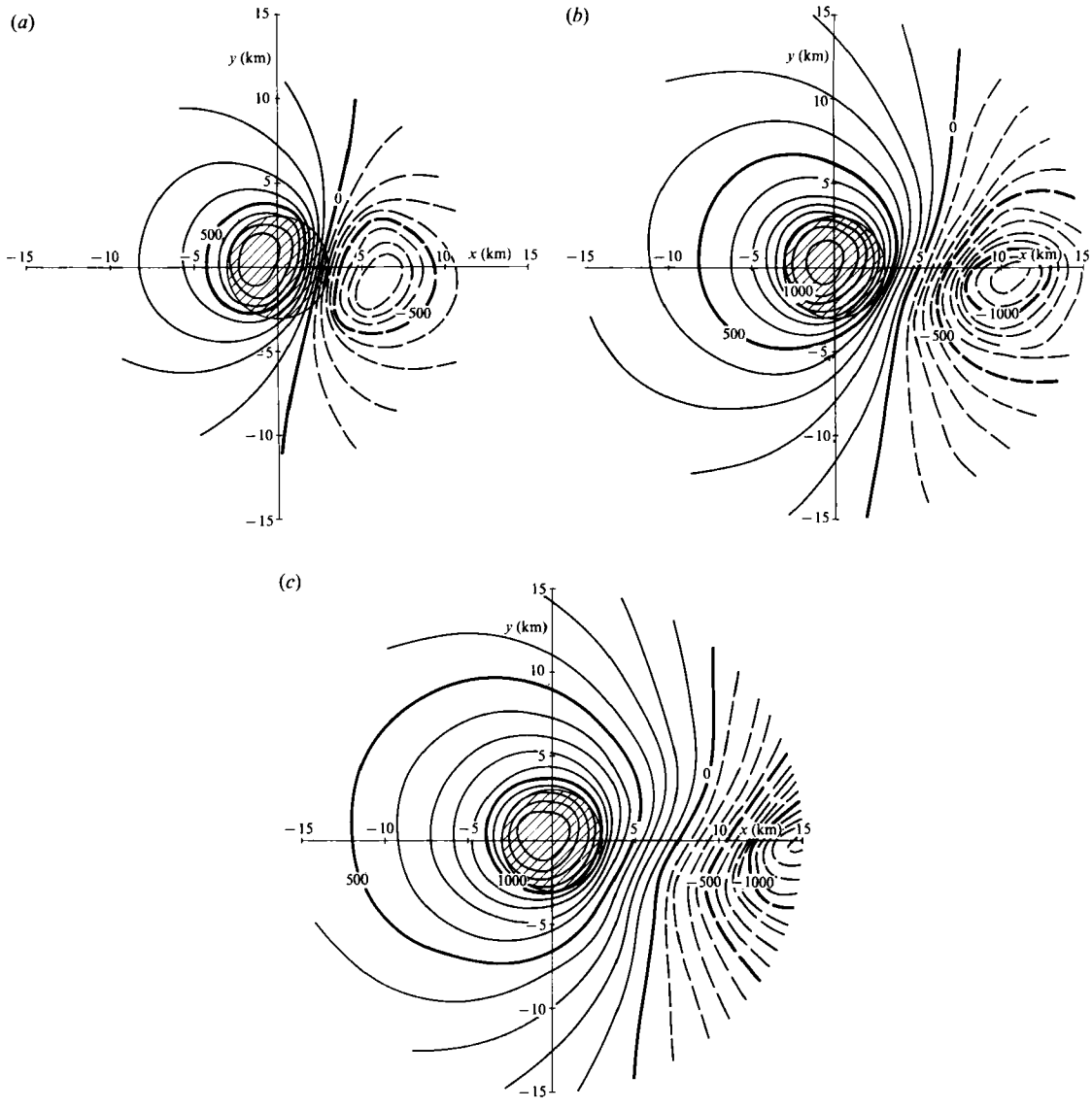

FIGURE 9. As figure 8, but for a larger upstream velocity, $u_0 = 10$ cm/s. In this case the butterfly pattern is rotated by a small angle only, before the vortex shedding starts. The development of a bell-shaped cyclonic vortex over the obstacle while an anticyclonic vortex is shed downstream can be clearly seen. (*a*) $t = 5 \times 10^4$ s, (*b*) $t = 10^5$ s, (*c*) $t = 1.5 \times 10^5$ s.

parabolid presented by Johnson (1984) suggests that a regularly rotating butterfly pattern is a special property produced by cylindrical obstacles with sharp edges whereas for smooth obstacles the angular velocity varies with the distance from the centre. The possible effects of self-advection of the induced currents needs further investigation.

We interpret the pattern shown in figure 8(*d*) in H & B as the linear final state which has become stationary due to friction. This is supported by the similarity to figure 3.

In the fast case (F), see figure 5 in H & B, the evolution of the response pattern

is quite similar to the quasi-nonlinear approximation shown in figure 9. One can clearly identify the linear initial phase dominated by a rotating butterfly structure and the advective phase where the upwelling area is shifted to the top of the obstacle, whereas the downwelling area leaves the topographic feature. The long tail of the warm area found by H & B is probably the result of a nonlinear vortex–vortex interaction which is disregarded in the quasi-nonlinear approach.

These findings show that the essential dynamics of the response pattern forced by isolated topographic features can be reasonably described by a quasi-nonlinear theory.

7. Discussion

An analytical investigation of the response of a stratified f-plane ocean to small topographic features is presented. A time-dependent upstream current flowing over ridges and cylindrical obstacles has been studied in a quasi-nonlinear approach in the framework of the quasi-geostrophic theory, which gives a sufficient description of the response scenario. Apart from a few exceptions we confine the analysis to an inviscid ocean.

In order to solve the vorticity equation we have derived an integral equation based on a Green's function method which covers the whole response scenario. In particular, the linear response in the starting phase and the nonlinear final state appear as limit cases. The boundary conditions are accounted for automatically. Thus, once the Green's function is known the solution to various examples of upstream flows and topographical features can be calculated in a straightforward manner.

By means of the analytical treatment an explicit indication of terms responsible for generation of topographic waves, vortex shedding, and final steady states is possible and thus a further elucidation of those processes is achieved.

In the case of infinitely long ridges the response scenarios are completely governed by vortex formation over the feature and vortex shedding. Such a choice of geometry filters out topographical waves. It is found that the solutions of the quasi-nonlinear theory obey even the full nonlinear quasi-geostrophic vorticity equation. The gross behaviour of the response has been illustrated in terms of density anomalies. The shape of the isolines mirrors basically the form of the bottom profile. For truncated profiles there are exponential terms with e-folding distances given by the Rossby radii, which smooth out the pattern over abrupt changes of the topography.

The case of cylindrical obstacles is, in particular in the starting phase, significantly affected by topographic waves. These waves have a 'butterfly structure' formed by positive and negative density anomalies and rotate clockwise round the feature. A topographic frequency emerges which is determined by the inertial frequency, stratification and geometry of the feature.

For a background flow switched on suddenly and being constant thereafter the response is initially well described by the linear theory. For times of the order of the advection time, however, the linear theory no longer applies. Nevertheless there are some cases which are described by linear dynamics. For example, if friction is taken into account and provided the inverse damping rate is smaller than the advection time, then a damped topographic wave follows which approaches a stationary state before vortex shedding can develop. Moreover, for a forcing of not too long a duration or a periodic forcing with not too small a frequency the linear wave-type

solutions apply. As the examples discussed reveal, the time behaviour of those forced topographic waves can be rather complex.

Otherwise the process of vortex shedding comes into play, which disperses the topographic waves and leads to a stationary vortex pattern over the feature while a second vortex with opposite sign drifts downstream with the background flow. Thus topographic waves are only supported as long as the geostrophic currents associated with the disturbances have non-zero components normal to the feature. This is the case as long as the downstream-drifting vortex has not left the area of the feature.

Baroclinic and barotropic contributions to the response pattern exhibit the same shaped contour lines but the scales differ considerably owing to the different values of the Rossby radii R_0 and R_1. Stratification tends to enhance the topographic frequency f_{top}. Thus, the butterfly structure rotates faster and the vortex which will be shed downstream is displaced further perpendicular to the background flow as in the absence of stratification.

The theory is limited in several important ways. The topographic height, h, is assumed to be small compared to the depth, and changes in depth are taken into account in derivatives of h only. Thus transport over the features is only correct up to orders of h/H. Moreover, in the numerical scheme used to describe the vortex shedding an approximated Green's function has been taken into account, see Appendix B.

Nevertheless, the analytical quasi-nonlinear model can reproduce the dominant features found in numerical simulations, e.g. in H & B, remarkably well, and this agreement suggests that the model contains much of the essential dynamics of the phenomenon.

The analysis was focused on obstacles but the case of trenches or canyons can easily be included by changing the sign of the function $h(x, y)$ whieh describes the topographic feature.

There are many papers suggesting relatively strong influences of small topographic features on the dynamics of an ocean even far from the bottom. For example, Owens & Hogg (1980) found evidence of stratified Taylor columns at 36° N, 55° W in agreement with the models of Hogg (1973) and Huppert (1975). Freeland & Denman (1982) reportcd a well-documented example of a topographically controlled upwelling centre off southern Vancouver Island, which occurs every spring in response to the development of a coastal current. As a result of the NOAMP experiments Mittelstaedt (1986) reported a strong influence of the bottom topography on the dynamics of the West European Basin. They found topographically trapped currents which, in accordance with theory, form anticyclonic eddies over hills and cyclonic eddies over valleys.

Series of satellite images collected by Horstmann (1983) reveal that the Arkona Basin in the Baltic Sea is populated by eddies. There are some topographic features favourable for vortex generation in that area and the numerical examples given in the present paper correspond to certain features of the basin. However, there are various irregularities in the coastline geometry which may also act as eddy generators.

In summary, it seems that the observational findings give indications rather than evidence for the theoretically predicted response patterns and scenarios. Thus we suggest further process-oriented field work, e.g. in the Arkona Basin, in order to study the effects of small topographic features.

Appendix A. Evaluation of the Green's function

In order to solve the integro-differential equation (3.20) we have to calculate the Green's function involved, which according to §3.3 is subject to

$$(\nabla^{2\prime}+\mathscr{L}')\,\bar{\mathscr{D}}_{t'}\,G(\boldsymbol{r},z,t,\boldsymbol{r}',z',t')=\delta(\boldsymbol{r}-\boldsymbol{r}')\,\delta(z-z')\,\delta(t-t') \tag{A 1}$$

with the boundary conditions

$$G\to 0 \quad \text{for} \quad r'\to\infty, \tag{A 2a}$$

$$G=0 \quad \text{for} \quad t<t', \tag{A 2b}$$

$$\left(\frac{\partial}{\partial z'}+\frac{N^2}{g}\right)\bar{\mathscr{D}}_{t'}\,G=0 \quad \text{for} \quad z'=0 \tag{A 3a}$$

$$\frac{\partial}{\partial z'}\bar{\mathscr{D}}_{t'}\,G=0 \quad \text{for} \quad z'=-H. \tag{A 3b}$$

We attack the problem with the ansatz

$$G(t,t')=\theta(t-t')\,K(t,t'). \tag{A 4}$$

As was shown in §3.3 the function $K(t,t')$ is governed by the equation

$$\bar{\mathscr{D}}_{t'}\,K(t,t')=0 \tag{A 5}$$

and fulfills the condition

$$K(t,t')|_{t=t'}=\mathscr{K}. \tag{A 6}$$

The function $\mathscr{K}$ is independent of time and obeys the boundary-value problem

$$(\nabla^{2\prime}+\mathscr{L}')\,\mathscr{K}(\boldsymbol{r},z,\boldsymbol{r}',z')=\delta(\boldsymbol{r}-\boldsymbol{r}')\,\delta(z-z'), \tag{A 7}$$

$$\left(\frac{\partial}{\partial z'}+\frac{N^2}{g}\right)\mathscr{K}=0 \quad \text{for} \quad z'=0, \tag{A 8a}$$

$$\frac{\partial}{\partial z'}\mathscr{K}=0 \quad \text{for} \quad z'=-H. \tag{A 8b}$$

We assume a small height of the isolated topographic feature, i.e. $h/H\ll 1$ and approximate the boundary condition (A 8b) by the flat-bottom condition

$$\frac{\partial}{\partial z'}\mathscr{K}=0 \quad \text{for} \quad z'=-H_0. \tag{A 9}$$

Then vertical and horizontal coordinates can be separated:

$$\mathscr{K}(\boldsymbol{r},z,\boldsymbol{r}',z')=\sum_n F_n(z)\,F_n(z')\,\Lambda_n(\boldsymbol{r}\cdot\boldsymbol{r}'), \tag{A 10}$$

where the F_n are the vertical eigenfunctions of the flat-bottom case, which are subject to the vertical eigenvalue problem

$$\left(\frac{\mathrm{d}}{\mathrm{d}z}\frac{1}{N^2}\frac{\mathrm{d}}{\mathrm{d}z}+\lambda_n^2\right)F_n(z)=0,$$

with $F_n'(0)=-(N^2/g)\,F_n(0)$ and $F_n'(-H_0)=0$.

For simplicity we confine ourselves to a constant Brunt–Väisälä frequency, where the eigenfunctions and eigenvalues follow as

$$F_0(z) = \frac{1}{H_0^{\frac{1}{2}}}\left(1-\frac{N^2}{g}\left(z+\frac{z^2}{H_0}\right)\right), \quad \lambda_0 = \frac{1}{(gH_0)^{\frac{1}{2}}} \tag{A 11}$$

and

$$F_n(z) = (2/H)^{\frac{1}{2}}\cos\left(\frac{n}{H_0}\pi z\right), \quad \lambda_n = \frac{n\pi}{NH_0}, \quad n \geqslant 1. \tag{A 12}$$

The eigenfunction $F_n(z)$ and the eigenvalues λ_n, as given by (A 11) and (A 12) are obtained by Taylor expansion of the full expressions with respect to the small parameter N^2H_0/g, or, equivalently R_1^2/R_0^2, see e.g. Fennel & Lass (1989). Here $R_n = (f\lambda_n)^{-1}$ is the Rossby radius associated with the nth mode. In particular R_0 is the barotropic or external Rossby radius and R_1 is the baroclinic or internal Rossby radius. According to (A 12) we have $R_n = R_1/n$.

Inserting (A 10) into (A 7) yields for Λ_n the equation

$$\left(\nabla^{2\prime}-\frac{1}{R_n^2}\right)\Lambda_n(\boldsymbol{r},\boldsymbol{r}') = \delta(\boldsymbol{r}-\boldsymbol{r}'). \tag{A 13}$$

The solution to (A 13) is the modified Bessel function K_0:

$$\Lambda_n(\boldsymbol{r},\boldsymbol{r}') = -\frac{1}{2\pi}K_0(|\boldsymbol{r}-\boldsymbol{r}'|/R_n). \tag{A 14}$$

Now we return to our original problem, the solution of the differential equation (A 5). It can easily be seen that for a homogeneous upstream flow $\boldsymbol{u}_0 = (U_0(t),0)$ any function of the form

$$X(\boldsymbol{r},t,\boldsymbol{r}',t') = X(\boldsymbol{r}-\boldsymbol{\alpha}(t),\boldsymbol{r}'-\boldsymbol{\alpha}(t'))$$

with

$$\boldsymbol{\alpha}(t) = \int_0^t \mathrm{d}\tau\, \boldsymbol{u}_0(\tau)$$

solves (A 5). This implies that in the quasi-nonlinear case the Green's function for a homogeneous upstream flow is

$$G(\boldsymbol{r},z,t,\boldsymbol{r}',z',t') = \theta(t-t')\,K(\boldsymbol{s},z,\boldsymbol{s}',z')$$

with

$$K(\boldsymbol{s},z,\boldsymbol{s}',z') = -\sum_n F_n(z)\,F_n(z')\frac{K_0(|\boldsymbol{s}-\boldsymbol{s}'|/R_n)}{2\pi}, \tag{A 15}$$

where $\boldsymbol{s}$ denotes the vector $\boldsymbol{s} = \boldsymbol{r}-\boldsymbol{\alpha}(t)$.

The Green's function L needed in the linear approximation follows for $\boldsymbol{\alpha}\to 0$ as

$$L(\boldsymbol{r},z,t,\boldsymbol{r}',z',t') = \theta(t-t')\,K(\boldsymbol{r},z,\boldsymbol{r}',z'), \tag{A 16}$$

i.e. in the linear initial phase K becomes independent of time. According to (3.26) the Green's function S which is needed in the nonlinear stationary case is

$$S(\boldsymbol{r},z,\boldsymbol{r}',z') = K(\boldsymbol{r},z,\boldsymbol{r}',z'). \tag{A 17}$$

For later reference we note the following useful standard relations of modified Bessel functions:

$$K_0\left(\frac{1}{R_n}|\boldsymbol{s}-\boldsymbol{s}'|\right) = \sum_{m=-\infty}^{\infty} \mathrm{e}^{\mathrm{i}m(\varphi-\varphi')}g_{mn}(s,s'), \tag{A 18}$$

where g_{mn} is defined by

$$g_{mn}(s,s') = \theta(s-s')\,K_m\left(\frac{s}{R_n}\right)I_m\left(\frac{s'}{R_n}\right)+\theta(s'-s)\,I_m\left(\frac{s}{R_n}\right)K_m\left(\frac{s'}{R_n}\right). \tag{A 19}$$

Here I_m and K_m are the modified Bessel functions of mth order, see e.g. Abramowitz & Stegun (1984). From the properties of K_m and I_m it follows that

$$g_{mn} = g_{-mn}.$$

From (A 18) follows the Fourier-series of L:

$$L(\boldsymbol{r},z,t,\boldsymbol{r}',z',t') = \theta(t-t')\sum_{m=-\infty}^{\infty}\frac{\mathrm{e}^{\mathrm{i}m(\varphi-\varphi')}}{2\pi}L_m(\boldsymbol{r},z,\boldsymbol{r}',z') \tag{A 20}$$

with

$$L_m(\boldsymbol{r},z,\boldsymbol{r}',z') = -\sum_n F_n(z)\,F_n(z')\,g_{mn}(r,r'). \tag{A 21}$$

Moreover we note

$$\int_{-\infty}^{\infty}\frac{\mathrm{d}y}{2\pi}K_0\left(\frac{1}{R_n}|s-s'|\right) = \tfrac{1}{2}R_n\exp\left(-|x-\varkappa(t)-(x'-\varkappa(t'))|/R_n\right). \tag{A 22}$$

Appendix B. Numerical solution of the quasi-nonlinear equation

In order to solve (6.4) numerically we first introduce a discrete time grid

$$\psi_n(\boldsymbol{r},z) = \Psi(\boldsymbol{r},z)-\Psi_n(\boldsymbol{r},z)+\sum_{i=1}^{n-1}\Delta t\,hf\int_0^{2\pi}\mathrm{d}\varphi'\,K_{\varphi',ni}(\boldsymbol{r},a)\,\psi_i(a,-H)$$
$$+\tfrac{1}{2}\Delta t hf\int_0^{2\pi}\mathrm{d}\varphi'\,K_{\varphi',nn}(\boldsymbol{r},a)\,\psi_n(a,-H), \tag{B 1}$$

where the subscripts n and i indicate the times $t = n\Delta t$ and $t' = i\Delta t$ with Δt being the time step. Note that the first term on the right-hand side is independent of time. When iterating (B 1) we see that in the nth step the first three terms on the right-hand side are known from the foregoing, $(n-1)$th, step and the problem amounts to the solution of a Fredholm-type integral equation with respect to φ, which has to be solved for each time step.

We simplify the problem further by taking into account only the barotropic part of the Green's function under the integral. Since in our case the barotropic Rossby radius is much larger than the radius of the obstacle, $R_0 \gg a$, the derivation of the Green's function reduces to

$$K_{\varphi',ni} = -\frac{1}{4\pi H_0}\frac{2as_{ni}\sin(\Phi_{ni}-\varphi')}{s_{ni}^2+a^2+2s_{ni}\,a\cos(\Phi_{ni}-\varphi')}, \tag{B 2}$$

where s_{in} and Φ_{in} are defined by

$$s_{ni}^2 = (x-(n-i)\,\Delta t\,U_0)^2+y^2, \quad \cos\Phi_{ni} = \frac{x-(n-i)\,\Delta t\,U_0}{s_{ni}}.$$

We proceed in two steps. First, we solve (B 1) at $r = a$ and $z = -H_0$, and then we insert the result again into (B 1) in order to evaluate the pressure field for arbitrary r and z.

It appears, that for $r = a$ the rightmost term on the right-hand side of (B 1) is a

Hilbert transform of the function ψ_n, where the Hilbert transform of a function $u(\alpha)$ is defined as

$$\boldsymbol{H}[u](\alpha) = \int_0^{2\pi} \frac{\mathrm{d}\varphi}{2\pi} \frac{\sin(\alpha-\varphi)}{1-\cos(\alpha-\varphi)} u(\varphi) \tag{B 3}$$

and has the useful property

$$\boldsymbol{H}[\boldsymbol{H}[u]](\beta) = -u(\beta) + \int_0^{2\pi} \frac{\mathrm{d}\varphi}{2\pi} u(\varphi). \tag{B 4}$$

This can be used to solve the Fredholm integral equation analytically. To this end we rewrite (B 1) as

$$\psi_n = \psi_n^I - \frac{\Delta t f h}{4H} \boldsymbol{H}[\psi_n]$$

with

$$\psi_n^I(a,\varphi,-H) = \psi_{0n}(a,\varphi,-H) + \frac{\Delta t f h}{2H_0} \sum_{i=1}^{n-1} \int_0^{2\pi} \frac{\mathrm{d}\alpha}{2\pi} \frac{2a s_{ni} \sin(\Phi_{ni}-\alpha)}{s_{ni}^2 + a^2 - 2 s_{ni} a \cos(\Phi_{ni}-\alpha)} \psi_i(a,\alpha,-H). \tag{B 5}$$

Applying the Hilbert transformation twice we arrive at

$$\psi_n(a,\varphi,-H) = \frac{\psi_n^I(\varphi) - \frac{\Delta t f h}{4H_0} \boldsymbol{H}[\psi_n^I](\varphi) + \left(\frac{\Delta t f h}{4H_0}\right)^2 \int_0^{2\pi} \frac{\mathrm{d}\varphi'}{2\pi} \psi_n^I(\varphi')}{1 + \left(\frac{\Delta t f h}{4H_0}\right)^2}. \tag{B 6}$$

This equation was solved numerically. The time step was chosen to be much less than the advection timescale. The computations were carried out on a PC.

REFERENCES

ABRAMOWITZ, M. & STEGUN, A. 1984 *Handbook of Mathematical Functions*. Verlag Harri Deutsch, Thun-Frankfurt.

FENNEL, W. & LASS, H. U. 1989 *Analytical Theory of Forced Oceanic Waves*. Berlin: Akademie-Verlag. 312 pp.

FREELAND, H. L. & DENMAN, K. L. 1982 A topographically controlled upwelling center off southern Vancouver Island. *J. Mar. Res.* **42**, 1069–1093.

GILL, A. E., DAVEY, M. K., JOHNSON, E. R. & LINDEN, P. F. 1986 Rossby adjustment over a step. *J. Mar. Res.* **44**, 713–738.

GOULD, W. J., HENDRY, R. & HUPPERT, H. E. 1981 An abyssal topographic experiment. *Deep-Sea Res.* **28** A, 409–440.

HOGG, N. G. 1973 On the stratified Taylor column. *J. Fluid Mech.* **58**, 517–537.

HORSTMANN, U. 1983 Distribution patterns of temperature and water colour in the Baltic Sea as recorded in satellite images: Indicator for phytoplankton growth. *Ber. IfM Kiel*, No. 106, 147 pp.

HUPPERT, H. E. 1975 Some remarks on the initiation of inertial Taylor columns. *J. Fluid Mech.* **67**, 397–412.

HUPPERT, H. E. & BRYAN, K. 1976 Topographically generated eddies. *Deep-Sea Res.* **23**, 655–679 (referred to herein as H & B).

JOHNSON, E. R. 1984 Starting flow for an obstacle moving transversely in a rapidly rotating fluid. *J. Fluid Mech.* **149**, 71–88.

KILLWORTH, P. 1989 How much of a baroclinic coastal Kelvin wave gets over a ridge? *J. Phys. Oceanogr.* **19**, 1131–1148.

McCartney, M. S. 1975 Inertial Taylor columns on a β-plane. *J. Fluid Mech.* **68**, 71–95.

Mittelstaedt, E. 1986 Ausbreitungsbedingungen für Stoffe in grossen Ozeantiefen. *DHI Report*, Hamburg, 202 pp.

Owens, W. B. & Hogg, N. H. 1980 Oceanic observations of stratified Taylor columns near a bump. *Deep-Sea Res.* **27** A, 1029–1045.

Verron, J. 1986 Topographic eddies in temporally varying oceanic flows. *Geophys. Astrophys. Fluid Dyn.* **35**, 257–276.

Verron, J., Provost, C. le & Holland, D. W. R. 1987 On the effects of a midocean ridge on the general circulation: numerical simulation with an eddy-resolving ocean model. *J. Phys. Oceanogr.* **17**, 301–312.

Willmott, A. J. 1984 Forced double Kelvin waves in a stratified ocean. *J. Mar. Res.* **42**, 319–358.